MATERIALS SCIENCE

Tissue-adhesive hydrogel–MXene biosensor for in situ intraoral TNF-α detection

Tsz Hung Wong[1]†, Weijia Liu[2]†, Jiaoli Li[2], Jie Ma[1], Yijie Cheng[3], Ruihao Lu[4], Kent J. Koster[5], Jeffrey D. Cirillo[5], Xinyue Liu[3], Hajime Sasaki[6], Chenglin Wu[2]*, Shaoting Lin[1]*

Current dental care relies on subjective assessments or sophisticated diagnostics, both struggling to balance efficiency and accuracy. In situ biosensors offer a promising solution for real-time biomarker detection, yet their practical deployment in oral tissue is hindered by challenges in sensitivity, specificity, and stability due to low biomarker concentrations, molecular-level heterogeneity, and dynamic intraoral interactions. Here, we develop a tissue-adhesive hydrogel–MXene (TAHM) biosensor, integrating a graphene/MXene sensing probe, a tissue-adhesive patch, and a selective-permeable hydrogel membrane, for in situ detection of tumor necrosis factor–α, a proinflammatory cytokine. Our TAHM biosensor achieves high sensitivity with a limit of detection of 18.2 femtograms per milliliter, excellent selectivity with an interference coefficient below 7%, and mechanical stability with resistance variation under 0.5% under varying stretch ratio and loading rates. The sensor's performance is further validated through in vitro, in vivo, and ex vivo experiments. The work highlights the potential of in situ biosensor as a transformative tool for real-time oral diagnostics.

INTRODUCTION

Infection-induced oral inflammations, particularly pulpitis and periodontitis, can result in serious complications, including pulp necrosis, periodontal tissue destruction, and ultimately tooth loss (*1*, *2*). The inflammatory response, mediated by cytokines and other tissue-destructive mediators, plays a crucial role in this process (*3*, *4*). In disease management, similar to other chronic inflammatory diseases, early detection, prompt control of inflammation, and timely interventions are critical to preventing irreversible tissue destruction and functional loss (*5*, *6*). Therefore, these mediators have been recognized as important biomarkers for diagnosis and disease monitoring.

However, an empirical diagnostic and prognostic system for dental inflammation has not yet been established (*7*). In general, dental practice requires rapid examination and diagnosis at the point of care typically conducted on or near the dental chair. Current diagnosis mainly relies on patients' subjective narratives, routine clinical assessments (such as visual inspection, palpation, percussion, x-ray imaging, pulp vitality test, and periodontal pocket probing), and clinicians' expertise and experience (*8*). These subjective approaches may not accurately capture the true state of inflammation, potentially leading to misdiagnosis, subsequent over- or undertreatment, and ultimately, adverse clinical outcomes.

Laboratory-based analytical approaches, such as enzyme-linked immunosorbent assay (ELISA) for detecting proteins, polymerase chain reaction (PCR) for gene expression analysis, and profiling of microbiota, facilitate the quantitative assessment of clinically obtained biological samples, offering comprehensive insights into disease pathophysiology (*9*, *10*). However, these methods are often unsuitable for clinical dentistry, where immediate judgment is required, due to their lack of timeliness. Consequently, there is an increasing clinical demand for advanced point-of-care (POC) diagnostic tools that enable early disease identification, effective pathological management, and strategic treatment guidance (Fig. 1A) (*11*).

The cytokines in tissue exudates from periodontal tissues and dental pulp, which is a target of dental POC testing, is typically on the order of picograms per milliliter (*12*). The detection of such low-concentration proteins often requires labor-intensive and time-consuming procedures, such as ELISA (*9*, *10*). To examine localized inflammation directly, a sensor needs to be placed on the relevant area or its immediate vicinity; however, biosensors placed on oral tissues are inevitably subjected to dynamic oral movements, potentially leading to detachment or deformation along with sensing failure or signal distortion (*13*). In addition, the molecular complexity of oral fluids leads to the accumulation of nontarget biomolecules [e.g., proteins, enzymes, and microorganisms (*14*)] on the sensing surface, blocking target biomarker interaction with the sensor and compromising signal fidelity (*15*). Therefore, the requirements for oral POC testing include ease of use, noninvasiveness, reliable sampling, high sensitivity for low-concentration biomarkers, signal accuracy, and cost-effectiveness.

Here, we propose a clinically translatable tissue-adhesive hydrogel–MXene (TAHM) biosensor, consisting of a graphene/MXene sensing probe, a tissue-adhesive hydrogel (TAH) patch, and a selective-permeable hydrogel (SPH) membrane (Fig. 1B), as a POC diagnostic tool for oral inflammation. As an analytical device that converts biochemical events into electrical signals, this biosensor offers a promising solution to address the current challenges in sensitivity, selectivity, and robustness (*16*, *17*). Our TAHM sensor enables in situ detection of tumor necrosis factor–α (TNF-α) in the oral cavity with high sensitivity [limit of detection (LOD): 18.2 fg/ml], excellent selectivity (interference coefficient below 7%), and strain insensitivity (resistance variation below 0.5%). The enhanced sensitivity is attributed to the functionalized graphene/MXene sensing probe, where graphene enables efficient charge transport and high

[1]Department of Mechanical Engineering, Michigan State University, East Lansing, MI, USA. [2]Department of Civil & Environmental Engineering, Texas A&M University, College Station, TX, USA. [3]Department of Chemical Engineering and Materials Science, Michigan State University, East Lansing, MI, USA. [4]College of Natural Science, Michigan State University, East Lansing, MI, USA. [5]Center for Airborne Pathogen Research and Imaging, Texas A&M School of Medicine, Bryan, TX, USA. [6]Department of Cariology, Restorative Sciences & Endodontics, University of Michigan, Ann Arbor, MI, USA.
*Corresponding author. Email: chenglinwu@tamu.edu (C.W.); linshaot@msu.edu (S.L.)
†These authors contributed equally to this work.

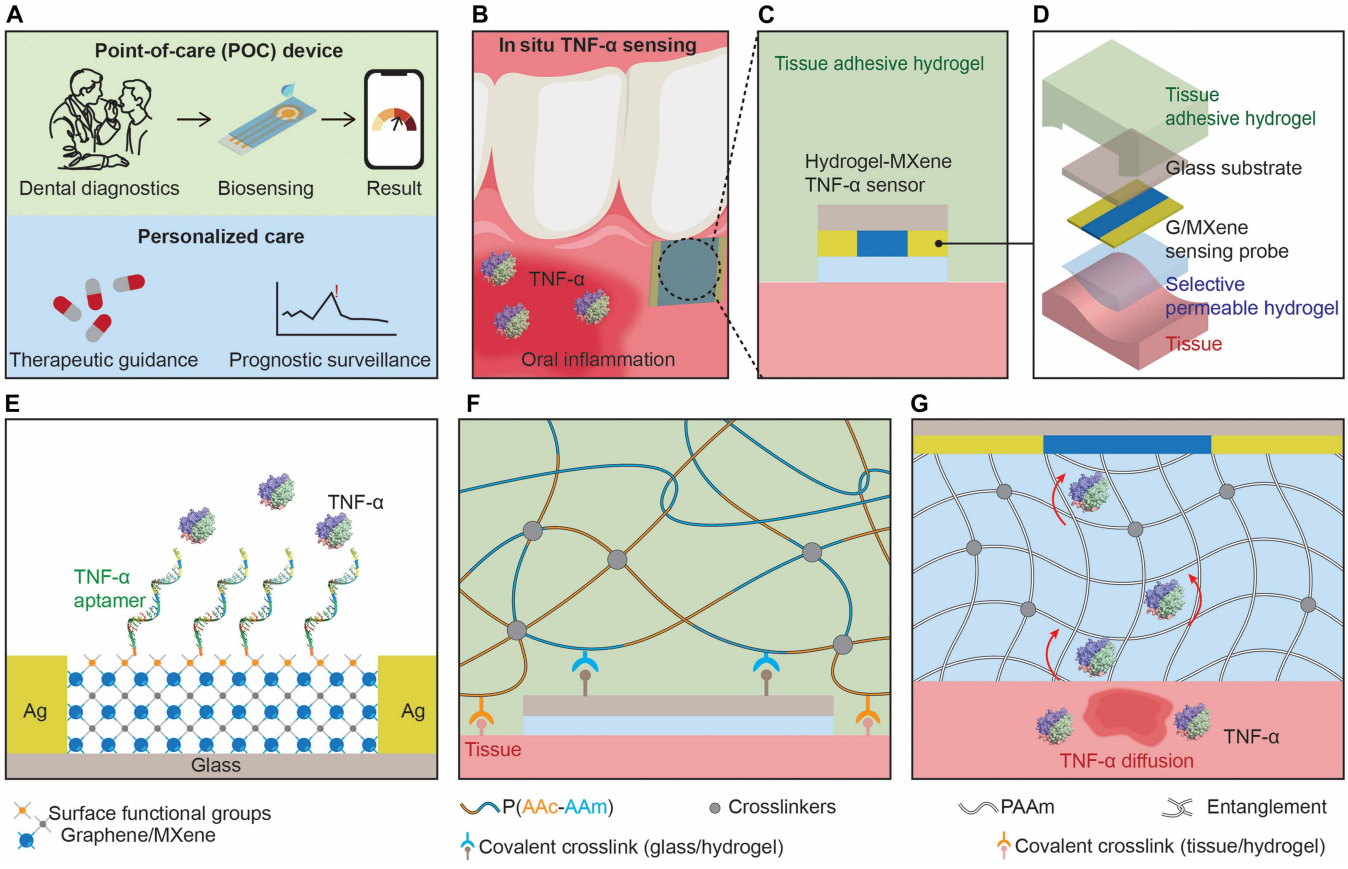

Fig. 1. Schematic illustration of the design of the TAH-MXene biosensor. (**A**) A POC biosensing device for use during dental examinations, where real-time biomarker analysis supports therapeutic decision-making and prognostic monitoring. (**B**) Operational scenario of the tissue-adhesive hydrogel-MXene (TAHM) biosensor adhered to gingival tissue near an inflammation site, enabling direct detection of tumor necrosis factor–α (TNF-α) in local oral fluids. (**C** and **D**) Cross-sectional sandwich structure of the TAHM biosensor, composed of (from top to bottom) a TAH patch, a graphene/MXene sensing probe on a glass substrate, and a selective-permeable hydrogel (SPH) membrane. (**E**) Schematic of the graphene/MXene sensing probe, which includes a glass substrate, silver electrodes, and a graphene/MXene layer functionalized with TNF-α–specific aptamers (VR11). (**F**) Polymer network of the TAH patch, comprising an entangled poly(acrylic acid–co–acrylamide) [P(AAc-co-AAm)] copolymer structure. N-hydroxysuccinimide (NHS) esters grafted onto the acrylic acid (AAc) component enable covalent bonding with wet tissue, while acrylamide (AAm) units form covalent linkages with the silane-treated sensor substrate (glass). (**G**) TNF-α molecules diffuse through the selectively permeable hydrogel membrane and reach the sensing surface.

charge sensitivity, while MXene provides a stable platform for immobilizing specific biomarker receptors, collectively improving sensitivity. The superior selectivity is achieved by the SPH membrane, which effectively filters nontarget biomolecules, while allowing target biomarkers to penetrate. The strain insensitivity is achieved through the mucoadhesive hydrogel patch, which provides robust adhesion to both the wet tissue and the sensor substrate while serving as a soft cushion to effectively reduce stress concentration and retard crack extension, attributed to the modulus mismatch between rigid biosensors and mucosal tissues. Comprehensive biosensor performance is supported by in vitro, ex vivo, and in vivo characterizations. Collectively, these validations support that our TAHM in situ biosensor enables real-time monitoring of tissue-derived oral biomarkers and holds strong promises for advancing POC diagnostics in personalized oral health management. The device can be seamlessly integrated into routine dental checkups, allowing clinicians to assess in-time oral inflammation levels alongside standard examinations.

RESULTS

Design of TAHM biosensor

As shown in Fig. 1 (C and D), the TAHM biosensor features a sandwich-like structure composed of a graphene/MXene sensing probe, an SPH membrane, and a TAH patch. First, to detect low-concentration TNF-α in tissue exudates, we fabricate a field-effect transistor (FET) integrated with a graphene/MXene-based sensing probe (Fig. 1E). Graphene, serving as the primary two-dimensional conductive layer, offers high charge carrier mobility and a tunable bandgap, essential for resolving subtle electrical signals (*18*). Complementing graphene, MXene, a metal carbonitride material (*19*) enhances charge transfer efficiency and offers abundant surface functional groups (e.g., hydroxyl and carboxyl) (*20*), which serve as active sites for the covalent immobilization of TNF-α aptamers (VR11), thereby improving detection specificity. As the interface, MXene provides stable probe anchoring through its rich surface chemistry while preserving graphene's intrinsic carrier mobility by spatially decoupling the sensing region from the conductive channel.

In addition, it strengthens electrostatic coupling and signal amplification, ultimately enhancing the sensing sensitivity and mechanical robustness of the graphene/MXene FET biosensor, as validated by our previous research demonstrating its distinctive electrochemical performance in biosensing applications (*21*). On the other hand, FET-based biosensors enable rapid and ultrasensitive detection by transducing biomolecular interactions into electrical signals through gate field modulation (table S1) (*22*–*28*), where small local charge changes directly alter the carrier density in the semiconductor channel, leading to strong signal amplification (*29*). Minor electrical perturbations induced by TNF-α binding events are detectable, as evidenced by a distinct Dirac point shift in its electrical output. This integration of superior electronic properties and robust aptamer functionalization enables sensitive and specific TNF-α detection, even at trace concentrations in tissue exudates. In addition, one of the key advantages of in situ detection is its capacity to eliminate inaccuracies associated with limited oral fluid volume and sample contamination during collection. Second, to enable selective sensing of the target biomarker in complex biological environments, we synthesize an SPH membrane, composed of polyacrylamide (PAAm) that selectively blocks large nontarget biomolecules while allowing target biomarkers to penetrate, by tuning the polymer network's mesh size (Fig. 1G). Acting as a molecular sieve, the SPH membrane minimizes biofouling by physically isolating nontarget biomolecules from the sensing probe, which prevents the degradation of sensing performance. Third, to establish a mechanically stable sensing environment, we further design a TAH patch that consists of a highly entangled copolymer network, poly(acrylic acid–co–acrylamide) [P(AAc-co-AAm)]. Specifically, acrylic acid (AAc) monomers functionalized with *N*-hydroxysuccinimide (NHS) esters form covalent bonds with wet tissue surfaces, enabling robust adhesion. Meanwhile, acrylamide (AAm) monomers establish covalent linkages with the modified biosensor substrate [covalent bonds formed between PAAm and 3-(trimethoxysilyl)propyl methacrylate (TMSPMA)–functionalized glass and between NHS groups and amine-functionalized polyimide (PI) substrates] and enhance the bulk mechanical strength through the formation of highly entangled polymer networks (Fig. 1F). Under mechanical stress, this entangled polymer network deforms and slides, effectively distributing applied forces to maintain structural stability. This TAH patch acts as a soft cushion, reducing stress concentration from external tissue deformation and retarding crack extension at multiple interfaces caused by modulus mismatch between rigid biosensor and soft tissue. The synergy of interfacial bonding chemistries and bulk dissipation mechanism ensures the stable functionality of our TAHM biosensor in dynamic and wet oral environment.

Design of SPH membrane

One of the key factors in minimizing interference from nontarget biomolecules in complex biological environments is the incorporation of an SPH membrane (Fig. 2A). These impurities can adsorb onto the sensing probe through physical interactions (*30*), chemical bonding (*31*), or biological interactions (*32*), thereby hindering the detection of target biomarkers (Fig. 2B, left). This phenomenon, known as biofouling, is a pervasive challenge in biosensor applications, leading to compromised sensing accuracy and reduced sensor longevity (*33*, *34*). To address this challenge, we synthesize an SPH membrane to coat the sensing probe. It acts as a molecular sieve, selectively filtering out nontarget biomolecules and impurities with sizes notably larger than TNF-α, while permitting TNF-α molecules to freely interact with sensing probe (Fig. 2B, middle and right).

Design and characterization of the graphene/MXene sensing probe

Another key factor in enabling detection of low concentrations of TNF-α within the complex tissue exudate lies in the surface functionalization of the graphene/MXene sensing probe (Fig. 2C). Pristine graphene is first deposited on a glass substrate, followed by coating of an MXene nanolayer. Fourier transform infrared (FTIR) spectroscopy measurements are performed to validate the chemical modifications on MXene by identifying chemical bonds and characteristic functional groups (Fig. 2D and fig. S1). The broad band at 3420 cm^{-1} corresponding to the ─OH stretching and the peak at 1575 cm^{-1} corresponding to the ─C═O stretching confirm the effective MXene deposition. The morphology and structural changes of the graphene and MXene are further validated by scanning electron microscope (SEM) and x-ray diffraction (XRD) (fig. S3). The MXene nanolayer is sequentially functionalized with (3-aminopropyl)triethoxysilane (APTES) to introduce amino functionalities, as indicated by new bands at ~2900 cm^{-1} corresponding to symmetric and asymmetric $-CH_2$ vibrations and 1000 cm^{-1} corresponding to Si─O bonds; glutaraldehyde (GA) as a bifunctional cross-linker, as evidenced by the emergence of a 1690 cm^{-1} peak (C═N stretching), confirming Schiff base formation (*35*, *36*); and TNF-α aptamer (VR11), as indicated by additional bands at 800 and 870 cm^{-1} corresponding to nucleobase vibrations (Fig. 2C and fig. S3) (*37*). Upon binding TNF-α, the VR11 aptamer undergoes conformational folding into a guanine quadruplex structure (*38*), enhancing proximity to the MXene surface while preserving sensitivity and specificity. To ensure optimal performance under physiological ionic conditions, we use a short covalent APTES-GA linker for aptamer immobilization onto the MXene surface. Compared to conventional π-π stacking approaches, this strategy maintains aptamer proximity within the Debye length, preserves the high transconductance of the graphene channel, and improves sensing stability in high–ionic-strength environments (*39*).

Next, FET measurements reveal distinct Dirac point shifts after each functionalization step [Fig. 2, C (right) and E, and fig. S4, A and B], confirming that surface modifications influence doping behavior and thereby alter the electronic properties. Initially, MXene modification induces a leftward shift due to negatively charged surface groups (−OH, −O, and −F), which enhances hole doping in graphene, and also the hydrophilicity and provides favorable sites for ion solvation and desolvation. Subsequently, APTES functionalization causes a further leftward shift, likely resulting from a condensation reaction with MXene's hydroxyl groups, releasing H^+ ions and intensifying the p-type doping effect. In contrast, GA forms stable C═N bonds via Schiff base reactions with APTES but does not notably affect the Dirac point position. Last, immobilization of the TNF-α aptamer (VR11) leads to a rightward shift, attributed to the negatively charged phosphate backbone inducing an n-type doping effect by reducing hole concentration. Further evaluation by cyclic voltammetry (CV) (Fig. 2F) reveals that MXene incorporation reduces the electrochemical capacitance, as evidenced by a decrease in the enclosed CV curve area (inset in Fig. 2F). This change reflects altered interfacial electrochemical behavior and increased responsiveness to charge perturbations. The enhanced sensitivity is attributed to MXene's high surface activity and distinctive charge distribution, which collectively minimize charge accumulation

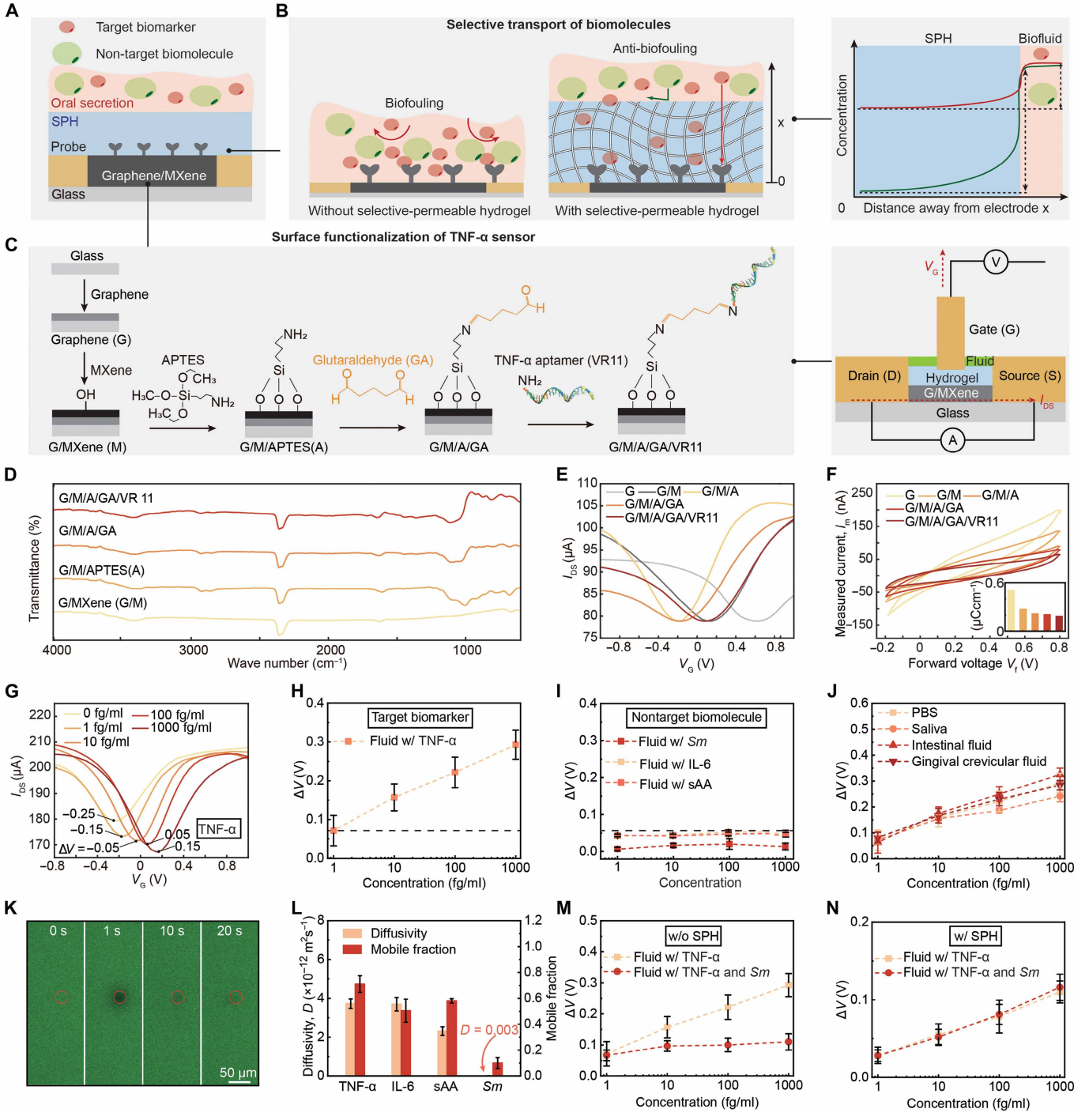

Fig. 2. Design, functionalization, and characterization of the TAHM biosensor. (**A**) Schematic of the TNF-α biosensor design. (**B**) Molecular engineering of the SPH membrane. (**C**) Surface functionalization of the graphene/MXene sensing probe. (**D** to **F**) Validation of successful probe functionalization using (D) Fourier transform infrared (FTIR) spectroscopy, (E) FET measurements, and (F) cyclic voltammetry (CV). (**G**) Transfer curves (I_D versus V_G) obtained in artificial biofluids with increasing TNF-α concentrations. (**H**) Dirac point shifts (ΔV) as a function of TNF-α concentration (in femtograms per milliliter), (**I**) as a function of *Streptococcus mutans* (*Sm*), interleukin-6 (IL-6), and salivary α-amylase (sAA) at varying concentrations. *Sm* concentration is expressed in ×250 colony-forming units (CFU)/ml, IL-6 concentration is expressed in femtograms per milliliter, and sAA concentrations are shown in milliunits per milliliter. The dashed lines in (H) and (I) indicate the response corresponding to TNF-α (1 fg/ml). All signals from nontarget biomolecules at their respective concentrations fall below this threshold. (**J**) Dirac point shifts (ΔV) as a function of TNF-α concentration in various artificial fluids, including phosphate-buffered saline (PBS), saliva, intestinal fluid, and gingival crevicular fluid (GCF). (**K**) Images of fluorescence recovery after photobleaching (FRAP) for TNF-α in an SPH membrane. (**L**) Summary of FRAP results for TNF-α, IL-6, sAA, and *Sm* within an SPH membrane with an average mesh size of ~6.9 nm, showing their corresponding average diffusivity and mobile fraction values. (**M** and **N**) Dirac point shifts (ΔV) in fluids with TNF-α alone and with both TNF-α and *Sm*, measured using TAHM biosensors (M) without and (N) with an SPH membrane. Values in [(H) to (J), (L), (M), and (N)] represent mean ± SD [$n = 4$ for (L); $n = 8$ for all others].

while improving signal transduction at the sensing interface. These improvements facilitate more precise TNF-α detection through strengthened surface interactions.

In vitro sensing characterization of the TAHM biosensor

Characterization of sensing sensitivity

To evaluate the sensing performance of the TAHM biosensors for TNF-α, we conduct a series of calibration experiments under various conditions. The TAHM biosensor is first characterized across a concentration range from 1 to 1000 fg/ml. As shown in Fig. 2G, when the drain-to-source voltage (V_{ds}) is maintained at 10 mV, the transfer curves shift positively with increasing TNF-α concentrations, indicating an n-type doping effect in graphene. This behavior results from the binding of TNF-α molecules to the functionalized surface, which perturbs the local charge distribution on the MXene layer. The induced charge redistribution modulates interfacial charge transfer, enhancing electron injection into the graphene channel. As a result, a higher positive gate voltage is required to reach the charge neutrality point, causing the transfer curve to shift rightward. The magnitude of the Dirac point shift correlates directly with TNF-α concentration, as illustrated in Fig. 2H. Specifically, the shift exhibits a linear relationship with the logarithm of TNF-α concentration, increasing from 0.07 to 0.29 V as the concentration rises from 1 to 1000 fg/ml, with a LOD of 2.9 fg/ml. This linear trend confirms that the sensor's electrical response is quantitatively proportional to TNF-α concentration, enabling precise and reliable detection across a broad dynamic range.

The oral cavity harbors a diverse bacterial flora, with 774 species identified to date (*40*). Given the presence of various impurities in human tissue exudates under practical conditions, a cariogenic oral bacterium *Streptococcus mutans* (*Sm*) (*41*), another cytokine interleukin-6 (IL-6), and salivary α-amylase (sAA) serve as control biomolecules. We next evaluate the specificity of the TNF-α sensor against them. Across a range of concentrations, all of them produce negligible signal variations, with all responses remaining below the lowest detected concentration of TNF-α (1 fg/ml) (Fig. 2I), indicating strong sensing specificity attributed to the specific binding between TNF-α and its aptamer (VR11). Take *Sm* as an example, it has a slope of approximately 0.0034 over a logarithmic concentration from 1× to 1000×. In contrast, TNF-α shows a slope of approximately 0.073 over a logarithmic concentration from 1× to 1000×. The ratio of these two slopes defines a selectivity coefficient of 21.5. Next, we assess the sensor's stability in physiologically relevant media, including phosphate-buffered saline (PBS), artificial saliva, intestinal fluid, and gingival crevicular fluid (GCF). As shown in Fig. 2J, the sensor consistently demonstrates stable responses across all media, maintaining a near-linear relationship between ΔV and the TNF-α concentration. These results underscore the sensor's reliability and its potential for quantitative TNF-α detection in diverse and physiologically complex environments, highlighting its potential for real-world biomedical applications.

Selectivity characterization of SPH membrane

Those nontarget biomolecules are then used to characterize their molecular diffusivity and mobility via fluorescence recovery after photobleaching (FRAP) within the SPH membrane (fig. S5). TNF-α exists as a trimer in solution, with a hydrodynamic diameter of ~5.6 nm and a molecular weight of ~15 kDa (*42*). In contrast, *Sm* exhibits an average diameter of 0.5 to 0.75 μm (*43*, *44*), while sAA and IL-6 have molecular weights of ~50 and ~25 kDa, respectively. Upon laser exposure, fluorescein isothiocyanate–labeled biomolecules undergo photobleaching, followed by diffusion-driven fluorescence recovery due to concentration gradients (Fig. 2K). Diffusivity is quantified by fitting the recovery curve using the Soumpasis model (*45*), while the mobile fraction is defined as the ratio of recovered fluorescence to initial intensity. As shown in Fig. 2L and fig. S6, in the SPH membrane with a mesh size around 6.9 nm (*46*), for smaller cytokines, TNF-α and IL-6, which have comparable hydrodynamic sizes, their diffusivities remain similar at ~3.7×10^{-12} m^2s^{-1}. In contrast, the slightly larger sAA exhibits moderately reduced diffusivity, (2.2×10^{-12} m^2s^{-1}). To further investigate the tunability of the SPH, we adjust its cross-linking density to obtain three variants with mesh sizes of ~6.9, 3.9, and 9.7 nm, respectively (fig. S6). The results reveal that all four molecules exhibit consistent trends in overall diffusivity and mobile fraction, while their absolute values vary systematically with changes in the hydrogel mesh size. The theoretical size-dependent comparison is illustrated in fig. S7 (*47*, *48*). Notably, we observe discernible differences in mobile fractions: approximately 0.7 for TNF-α, 0.5 for IL-6, 0.6 for sAA, and only 0.1 for *Sm*. This suggests that a larger portion of bacteria is restricted from diffusing into the bleached region, likely due to physical entrapment by the polymer network. In addition to molecular size, distinct interactions between the biomolecules and the hydrogel matrix can also contribute to the observed selectivity. These results demonstrate the hydrogel membrane's ability to facilitate selective biomarker diffusion while restricting microorganisms and other nontarget biomolecules. Considering that a certain level of moisture is present in the working environment of the SPH, we further evaluate its permeability toward the target biomarker under moderate swelling conditions (fig. S8). To better simulate the actual operating scenario, we encapsulated the SPH within a dry TAH layer and attached to a wet tissue. After a designated swelling period, the diffusivity and mobile fraction of TNF-α within the SPH are measured. The results show that after ~1 hour of swelling, both parameters remained almost unchanged, confirming that the SPH can be reliably used for biomarker detection in moist oral environments. This phenomenon can be attributed to several factors. First, there is a difference in water molecule capture efficiency between the pristine SPH and the dry TAH. Specifically, the driving force for water absorption is governed by the chemical potential gradient between materials, where the gradient between the SPH and the wet tissue is much smaller than that between the TAH and the wet tissue. When both are attached to a wet tissue, the dry TAH absorbs surface moisture much faster than the SPH, preventing the SPH from reaching a high degree of swelling. Second, the amount of available water is limited because a small piece of biological tissue does not continuously exude fluid. As a result, the SPH in direct contact with the tissue does not remain in a persistently swollen state. Third, confined swelling occurs because of the encapsulation by the TAH. Because the TAH tightly wraps around and robustly adheres to the tissue, the SPH can only swell to a limited extent. Collectively, these factors restrict the overall swelling of the SPH and, consequently, reduce the internal stress exerted on the TAH. This also mitigates the risk of delamination or detachment of the SPH during use. To further assess the selectivity of SPH, we develop an *Sm* sensor. As shown in fig. S9, the bare sensor generates electrical signals proportional to *Sm* concentrations, whereas application of the hydrogel membrane significantly suppresses the response, confirming its barrier function. Collectively, these findings highlight the hydrogel membrane's ability to

facilitate selective biomarker diffusion while restricting microbial interference, thereby enhancing biosensor selectivity and reliability in complex biological environments.

To further evaluate the effectiveness of the SPH membrane in enhancing sensing selectivity, we prepare a representative mixed fluid containing TNF-α and *Sm*, where the TNF-α concentration is verified while fixed *Sm* is maintained at a concentration of 2.5×10^5 colony-forming units (CFU)/ml. As depicted in Fig. 2M, in the absence of the hydrogel membrane, the TNF-α sensor's output signal at a given TNF-α concentration is significantly attenuated because of interference from *Sm*, with an interference coefficient of 80.4%. Interference coefficient is defined as the difference in the slope of sensing output across TNF-α concentrations between the pure TNF-α fluid and the TNF-α–*Sm* mixed fluid, normalized by the slope in the pure TNF-α fluid. Conversely, when a hydrogel membrane is applied, the TNF-α sensor exhibits minimal signal perturbation, with an interference coefficient of 7% (Fig. 2N). While a slight reduction in overall signal intensity is observed, likely due to partial diffusion hindrance of TNF-α through the membrane, this effect can be corrected during initial sensor calibration. Consequently, the LOD of the sensor with a hydrogel membrane increases from ~2.9 to 18.2 fg/ml. Critically, the hydrogel membrane facilitates selective interaction between the sensor and the target biomarker, enhancing specificity in complex biological environments. In addition, we perform identical experiments in heterogeneous solutions containing TNF-α mixed with IL-6 and sAA, respectively. Although the interfering effects of IL-6 and sAA are less pronounced than those of *Sm*, noticeable signal differences can still be observed (fig. S10A). Consistent with previous findings, the presence of the SPH barrier results in comparable output signals between pure TNF-α solutions and those containing interfering biomolecules (fig. S10B). We further test the biosensor in heterogeneous media based on various artificial biological fluids, including GCF, intestinal fluid, and saliva, while all of which exhibit the same trend (fig. S10, C to H). Our TAHM biosensor achieves the LOD of 18.2 fg/ml and maintains minimal signal interference below 7% in heterogeneous fluids, which is among the best compared to other TNF-α biosensors (table S2) (*49*–*53*). In addition, our TAHM biosensor stands among the few platforms capable of reliable sensing under in situ conditions. Its enhanced sensing performance stems from the synergy of material design on the graphene/MXene sensing probe and molecular design in the SPH membrane.

Hydrogels, as polymer networks infiltrated with a large quantity of water molecules, are regarded as ideal candidates for integrating with biosensors for enhanced sensing performance. For example, recent studies have leveraged the high water content and hydrophilic properties of hydrogels to facilitate the dissolution of target biomarkers in body fluids (*54*). In addition, ionic hydrogel systems have been used to mitigate biofouling, thereby enhancing the detection performance of biosensors (*54*–*57*). However, using the polymer network of hydrogels to filter and selectively screen biomolecules has not been thoroughly investigated. Here, we demonstrate that tuning the cross-linking density of hydrogels allows them to selectively block nontarget molecules by differentiating biomolecules based on size, thus minimizing their contact with the sensing probe. Our next step is to further study and design the hydrogel's composition and network to enable selective screening based on the reversible interactions or charge interactions with biomolecules, potentially expanding the Debye length (*15*), reducing surface capacitance (*58*), and lowering the LOD.

Characterization of TAH patch

The final key factor in ensuring stable sensing by minimizing interference from dynamic interactions lies in the TAH patch (Fig. 3A). This hydrogel patch is synthesized on a silane-treated glass substrate, where polymer chains form covalent cross-links with the surface (fig. S11) (*59*). As the hydrogel patch is further attached to wet tissues, it forms other covalent cross-links, following a dry adhesion process (*13*, *60*). As illustrated in Fig. 3B and fig. S12, when a dry hydrogel patch contacts wet tissue, it triggers fast water migration and then a phase transition from a dry, glassy state to a hydrated, rubbery state. During this process, the hydrogel patch initially adheres to the tissue surface through intermolecular bonding, followed by NHS esters reacting with primary amine groups present on the tissue surface, gradually forming NHS ester–amine coupling reaction (*61*). Concurrently, the hydrogel's mechanical properties change progressively, as water content increases. We define two critical parameters influencing the adhesive and mechanical performance of hydrogel patches: (i) hydration time (τ_h), where prolonged hydration time enhances water uptake, directly affecting the hydrogel's elasticity; and (ii) adhesion time (τ_a), where initial adhesion relies on the hydrogel's intrinsic stickiness, while covalent bond formation occurs over time, leading to fluctuations in adhesion strength before stabilization.

First, we evaluate the adhesion performance of the TAH patch (50 μm thick) by systematically varying the adhesion time (τ_a). A 90° peeling test (fig. S13) shows that the interfacial toughness between wet tissue (porcine skin) and a glass substrate increases with adhesion time (τ_a), from ~50 Jm^{-2} at 1 min to 350 Jm^{-2} at 7 min, until reaching a plateau (Fig. 3, C and D). This trend indicates that sufficient time is required for covalent bonds to form between the hydrogel and the wet tissue. Notably, our hydrogel adhesive can also exhibit on-demand detachment following the established protocol (*62*). Next, we examine the swelling behavior of the dry hydrogel patch under varying hydration times (fig. S14). For a hydrogel patch with an initial dry thickness (T_h) of 50 μm, its thickness progressively increases under free-swelling conditions, stabilizing at ~300 μm after 10 min. This steady-state thickness slightly exceeds its initial hydrated thickness of 250 μm. However, under limited water availability during adhesion, the hydrogel does not fully swell to its original thickness, indicating hydration constraints in practical applications. We further analyze the impact of hydrogel thickness on adhesive performance. As shown in Fig. 3E, increasing the dry hydrogel thickness from 50 to 200 μm significantly reduces interfacial toughness, decreasing from ~350 to 170 Jm^{-2}. Two primary factors are likely responsible for this trend. First, thicker hydrogels require more water for full hydration, yet surface moisture is often insufficient to induce the glassy-to-rubbery transition. Second, increased thickness enhances the rigidity of the dry hydrogel, reducing its ability to conform to the tissue surface and establish intimate contact. These two factors synergistically contribute to the reduction in adhesive performance with increasing hydrogel thickness.

Because this dry adhesion is intrinsically correlated with its hydration state, we further investigate how hydration affects its bulk properties. We first perform pure shear tensile testing on unnotched samples (Fig. 3F). As illustrated in Fig. 3G, increasing water content gradually reduces nominal stress while enhancing stretchability. At $\tau_h = 1$ min, the hydrogel exhibits a nominal stress of ~550 kPa and a stretchability of 2. As τ_h increases to 7 min, nominal stress decreases to ~300 kPa, while stretchability rises to 4.7. Concurrently, the Young's modulus decreases from around 850 to 250 kPa

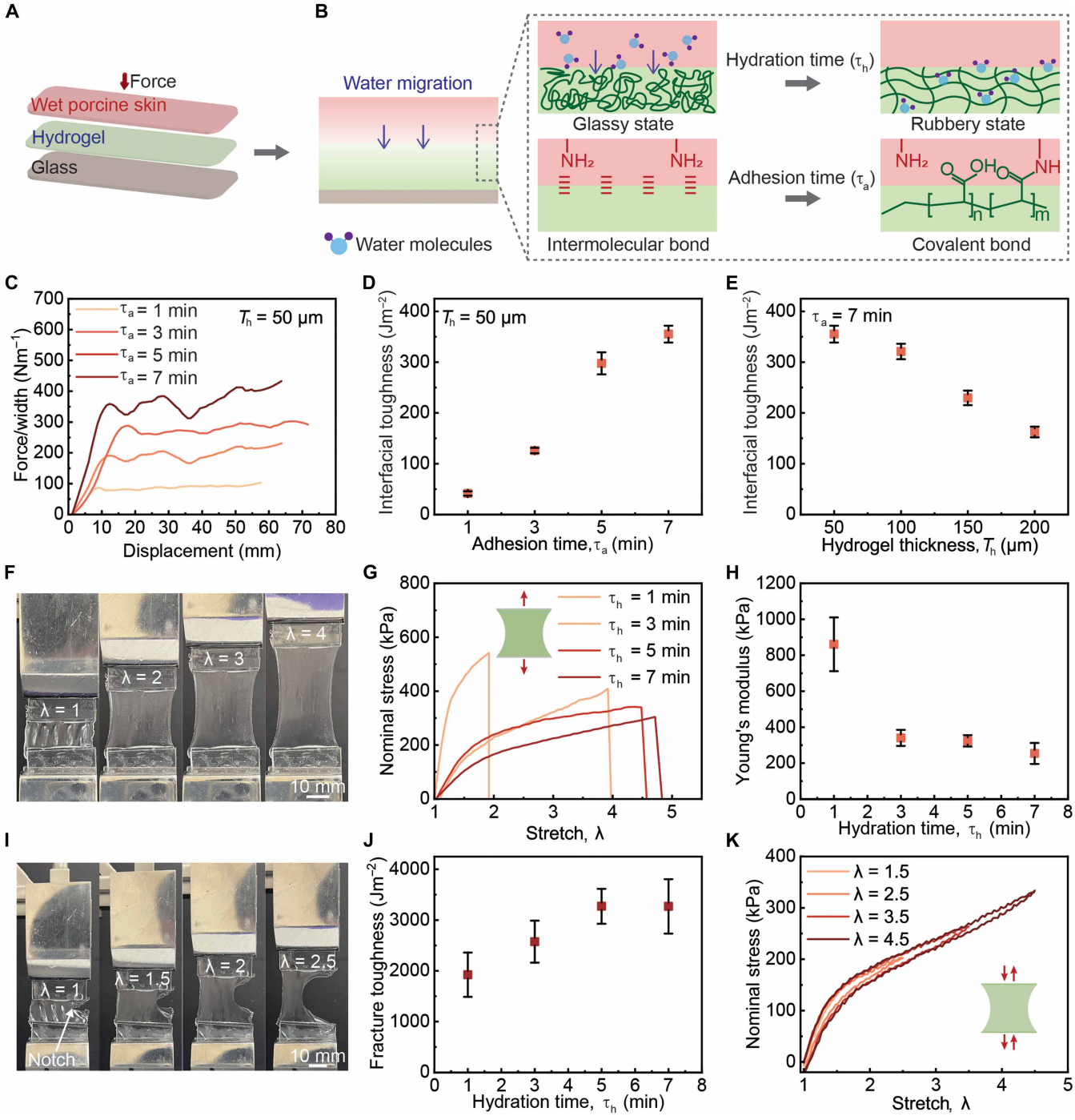

Fig. 3. Interfacial and bulk characterizations of the TAH patch. (**A**) Schematic illustration of a TAH patch adhered to wet tissue and a glass substrate. (**B**) Illustration of the adhesion mechanism during the hydration-induced phase transition, highlighting two control parameters: hydration time (τ_h) and adhesion time (τ_a). (**C**) Force-displacement curves from 90° peeling tests at various adhesion times (τ_a). (**D**) Interfacial toughness of TAH patches between wet tissue and glass at different adhesion times (τ_a). (**E**) Interfacial toughness as a function of hydrogel dry thickness (T_h). (**F**) Optical images of an unnotched TAH patch undergoing pure shear tensile testing. (**G**) Nominal stress as a function of hydration time (τ_h). (**H**) Young's modulus of the hydrogel at different hydration times (τ_h). (**I**) Optical images of a notched hydrogel patch during pure shear tensile fracture testing. (**J**) Fracture toughness of the hydrogel patch at varying hydration times (τ_h). (**K**) Nominal stress-stretch curves from loading-unloading cycles at different stretch levels for hydrogels hydrated for 7 min ($\tau_h = 7$). Scale bars, 10 mm [(F) and (I)]. Data in [(D), (E), (H), and (J)] represent mean ± SD ($n = 4$).

(Fig. 3H). These trends are attributed to increased polymer chain mobility, as water content rises during the dry-to-hydrated transition. However, these reductions do not indicate a decrease in overall mechanical robustness. To gain further insights, we conduct pure shear tensile testing on notched sample (Fig. 3I). As shown in Fig. 3J, fracture toughness increases from ~2000 to 3000 Jm^{-2}, indicating that fracture resistance improves along with the increased water content. We further perform loading-unloading cycle tests on unnotched samples, indicating a negligible hysteresis loop all over various stretches (Fig. 3K). This suggests that its toughening mechanism is likely not attributed to bulk hysteretic dissipation (*63*), but attributed to the chain entanglement that does not rely on large hysteresis (*64*, *65*).

Characterization of strain sensitivity

Next, we evaluate the sensor's stability under deformation induced by external mechanical stress, as the applied load inevitably alters its resistance, thereby affecting the stability of its output signal. These unintended resistance variations reduce sensing accuracy, distorting signals generated by actual biomarker concentration changes and potentially leading to inconsistent or erroneous outputs. To assess the performance of the TAHM sensor adhered to gingiva under stretching conditions, we simulate the scenario where the sensor is attached to gingival tissue (Fig. 4A). The structural analysis focuses on four key interfaces, arranged sequentially from top to bottom: (i) the interface between the TAH patch and glass substrate (TAH/Glass), (ii) the interface between the glass substrate and SPH membrane (Glass/SPH), (iii) the interface between the SPH membrane and tissue (SPH/Tissue), and (iv) the interface between the TAH patch and gingival tissue (TAH/Tissue). Among these, the TAH/Glass and TAH/Tissue interfaces are reinforced by covalent bonds, while the Glass/SPH and SPH/Tissue interfaces rely on physical attachments (Fig. 4B). Under tissue deformation, the TAH patch deforms along with the tissue, acting as a soft cushion to accommodate external stress. Among the four interfaces, those reinforced by covalent bonds demonstrate an interfacial toughness of ~350 Jm^{-2}, whereas interfaces relying on physical attachments exhibit a substantially lower interfacial toughness of around 1 Jm^{-2} (Fig. 4C). This pronounced disparity highlights the superior mechanical integrity enabled by our TAH patch, particularly under external stress and deformation.

To identify interfaces with a higher tendency for crack propagation, we calculate the energy release rates at each interface using finite element analysis (FEA). Without stabilization provided by the TAH patch, the energy release rates at the Glass/SPH and SPH/Tissue interfaces under a strain ratio of 1.5 are ~30 and 35 Jm^{-2}, respectively (Fig. 4, D and E). These values are orders of magnitude higher

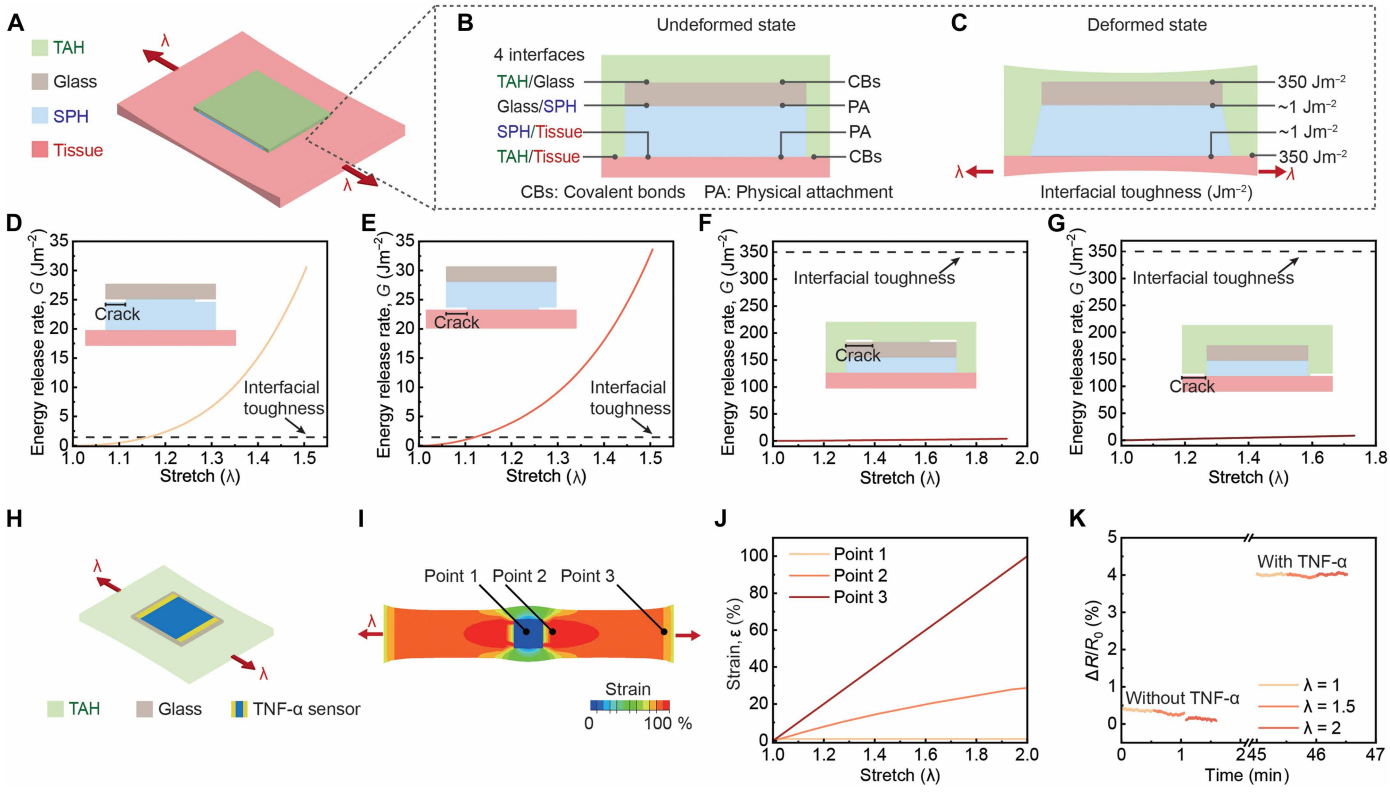

Fig. 4. Characterization of mechanical stability and strain sensitivity of the TAHM biosensor. (**A**) Schematic illustration of the TAHM biosensor adhered to gingival tissue under tensile deformation. (**B** and **C**) Schematics of the four interfacial layers within the TAHM biosensor in the (B) undeformed and (C) deformed states. (**D** and **E**) Comparison of energy release rates and corresponding interfacial toughness without the TAH patch at (D) the Glass/SPH interface and (E) the SPH/Tissue interface. (**F** and **G**) Comparison of energy release rates and interfacial toughness with the TAH patch at (F) the TAH/Glass interface and (G) the TAH/Tissue interface. (**H**) Schematic and (**I**) finite element analysis (FEA) of a TAHM biosensor under tensile strain, adhered via the TAH patch. (**J**) Local strain values at three positions (points 1, 2, and 3) within the TAHM biosensor plotted as a function of global stretch ratio λ. (**K**) Normalized resistance change ($\Delta R/R_0$) over time at different stretch levels, in the presence and absence of TNF-α. R_0 represents the resistance under the undeformed state without TNF-α.

than the adhesive strength provided by physical attachments at these interfaces (1 Jm^{-2}), indicating that there is potential crack propagation, leading to interface separation under mechanical deformation (fig. S17). In the presence of the TAH patch, the energy release rates at the Glass/SPH and SPH/Tissue interfaces are markedly reduced to ~0.3 Jm^{-2}, which is even lower than the interfacial toughness provided by the physical attachments. This substantial reduction mitigates the risk of separation at these interfaces (fig. S16). In addition, the energy release rates at the TAH/Glass and TAH/Tissue interfaces remain higher, at 4 and 8 Jm^{-2}, respectively. Although these values are relatively modest, they suggest that these two interfaces are more prone to detachment compared to the stabilized Glass/SPH and SPH/Tissue interfaces. To address this limitation, we introduced covalent cross-links at the TAH/Glass and TAH/Tissue interfaces, resulting in a marked increase in interfacial toughness to ~350 Jm^{-2} (Fig. 4, F and G). This value exceeds the energy release rates at all four interfaces by a substantial margin, effectively eliminating the risk of interface separation even under significant deformation. We also include the effect of SPH thickness on the overall TAHM biosensor, as shown in fig. S18. As the SPH thickness increases, the energy release rate at the SPH/Tissue and sensor Glass/SPH interfaces at $\lambda = 1.4$ gradually decreases, from ~15 and 33 Jm^{-2} at a thickness of 0.25 mm to below 2 Jm^{-2} when the thickness reaches 1 mm, and it remains stable even when the thickness increases to 5 mm. This reduction mainly results from the thicker hydrogel providing a larger energy dissipation zone, which better buffers and distributes energy at the crack tip during stress transmission. Taking into account both the energy release rate and the impact of SPH thickness on biomolecule diffusion time, we adopt a 0.1-mm-thick SPH membrane in our design. These findings underscore the critical role of covalent bonding in enhancing mechanical stability and ensuring reliable sensor performance under mechanical stress.

To analyze strain distribution across the TAHM biosensor during stretching (Fig. 4H), we perform FEA on the TAH patch and the sensor (movie S1), emphasizing three critical locations: point 1 at the sensing probe, point 2 at the TAH patch adjacent to the sensing probe, and point 3 at the TAH patch far away from the sensing probe (Fig. 4I). Under a global strain of $\lambda = 2$, point 1 experiences negligible strain, point 2 exhibits moderate strain (~30%), and point 3 experiences the greatest strain (~100%) (Fig. 4J). We further simulate the strain distribution in the TAHM biosensor without the TAH patch, exhibiting increased strain on the sensing probe during stretching (movie S2). These results demonstrate that the TAH patch can effectively reduce stress concentration, thus enhancing the overall mechanical stability of the TAHM biosensor. To evaluate whether this hydrogel patch deformation affects the sensor's output signal, we next subject this hydrogel patch, together with the attached sensor, to varying mechanical conditions, including different strain levels ($\lambda = 1$ to 2), stretching rates (0.1 to 1.5 Hz), and up to 500 stretching cycles. Across all tested conditions, the overall signal variation remains below 0.5%, indicating the sensor's exceptional stability during mechanical deformation (fig. S19). Last, we evaluate the sensor's sensing performance under deformation. The results indicate that mechanical deformation introduces minimal signal fluctuation (below 0.5%) without the presence of TNF-α. Upon exposure to TNF-α (1000 fg/ml), the sensor's signal increases to ~4%, remaining unaffected across various stretch levels. Through a combined analysis of simulations and experiments, we demonstrate the ability of the TAH patch to enhance the strain insensitivity of our TAHM biosensor, establishing it as a viable biosensing platform for real-world applications.

Ex vivo and in vivo sensing characterization of the TAHM biosensor

We further assess the sensing performance of the TAHM biosensor using ex vivo and in vivo characterizations. We first evaluate the biocompatibility of both TAH and SPH using a cell viability assay, and both hydrogels exhibit high cell viability exceeding 90% (fig. S20), indicating excellent biocompatibility suitable for subsequent in vivo demonstrations. We then evaluate its sensing performance in porcine gingiva with manually injected TNF-α fluid (Fig. 5A). We start with an assessment of the adhesion performance of TAH patch on porcine gingival tissue (Fig. 5B and fig. S21A). As shown in Fig. 5C, the peeling force initially exhibits a sharp increase and then remains steady throughout the peeling process. As the adhesion time (τ_a) increases, the peeling force correspondingly rises, from ~100 Nm^{-1} at $\tau_a = 1$ min to around 280 Nm^{-1} at $\tau_a = 7$ min. This trend is consistent with the adhesion test of the TAH patch between wet tissue and treated glass (Fig. 3C), demonstrating that a longer adhesion time leads to stronger adhesion due to the gradual formation of covalent bonds with the amine groups on the gingival tissue (*66*). In addition, our adhesive characterizations show a slight reduction of the interfacial toughness measured on porcine gingival tissue compared with that measured in porcine skin (Fig. 3D). This is likely due to the high modulus of gingival tissue [gingiva's modulus is ~165 kPa (*67*), compared to 40 kPa for skin (*68*)], because a stiffer tissue tends to contribute to lower energy dissipation than a softer tissue (*69*, *70*). Despite the reduction, the adhesive force remains greater than the energy release rate calculated in Fig. 4 (F and G), validating that this TAH patch is robust enough for subsequent in vivo characterization. To simulate the actual oral environment, which is characterized by limited moisture content and the presence of various biological impurities, we systematically investigate the adhesion performance of the TAH patch under different surface moisture conditions (fig. S21B) and in artificial saliva (fig. S21C). Experimental results demonstrate that the TAH exhibited consistent adhesive strength across varying levels of surface water content. Notably, stable adhesion is maintained even at a low water content of ~16.7 μl cm^{-2}. Furthermore, no significant difference is observed in adhesion performance between deionized (DI) water and artificial saliva, suggesting that the presence of physiological impurities does not adversely affect the adhesive properties of the hydrogel. Considering that certain tissue adhesives require external pressure during application to ensure effective bonding, we evaluate the adhesive performance of TAH under varying preloading pressures in a confined oral environment (fig. S22A). Notably, even without any applied pressure, the interfacial toughness between TAH and tissue reaches ~120 J m^{-2}. As the preloading pressure increases to 10 kPa, the interfacial toughness stabilizes at around 420 J m^{-2} (fig. S22B). These results suggest that only minimal pressure is needed to achieve conformal contact and stable adhesion, which is advantageous for use in restricted anatomical sites such as the oral cavity. Given the humid environment of the oral cavity, we also assess adhesion under aqueous conditions. Despite observable swelling, TAH maintains stable adhesion (fig. S23A), with interfacial toughness only slightly decreasing from ~420 to 320 J m^{-2} (fig. S23B). This toughness remains well above the critical energy release rates shown in Fig. 4 (F and G),

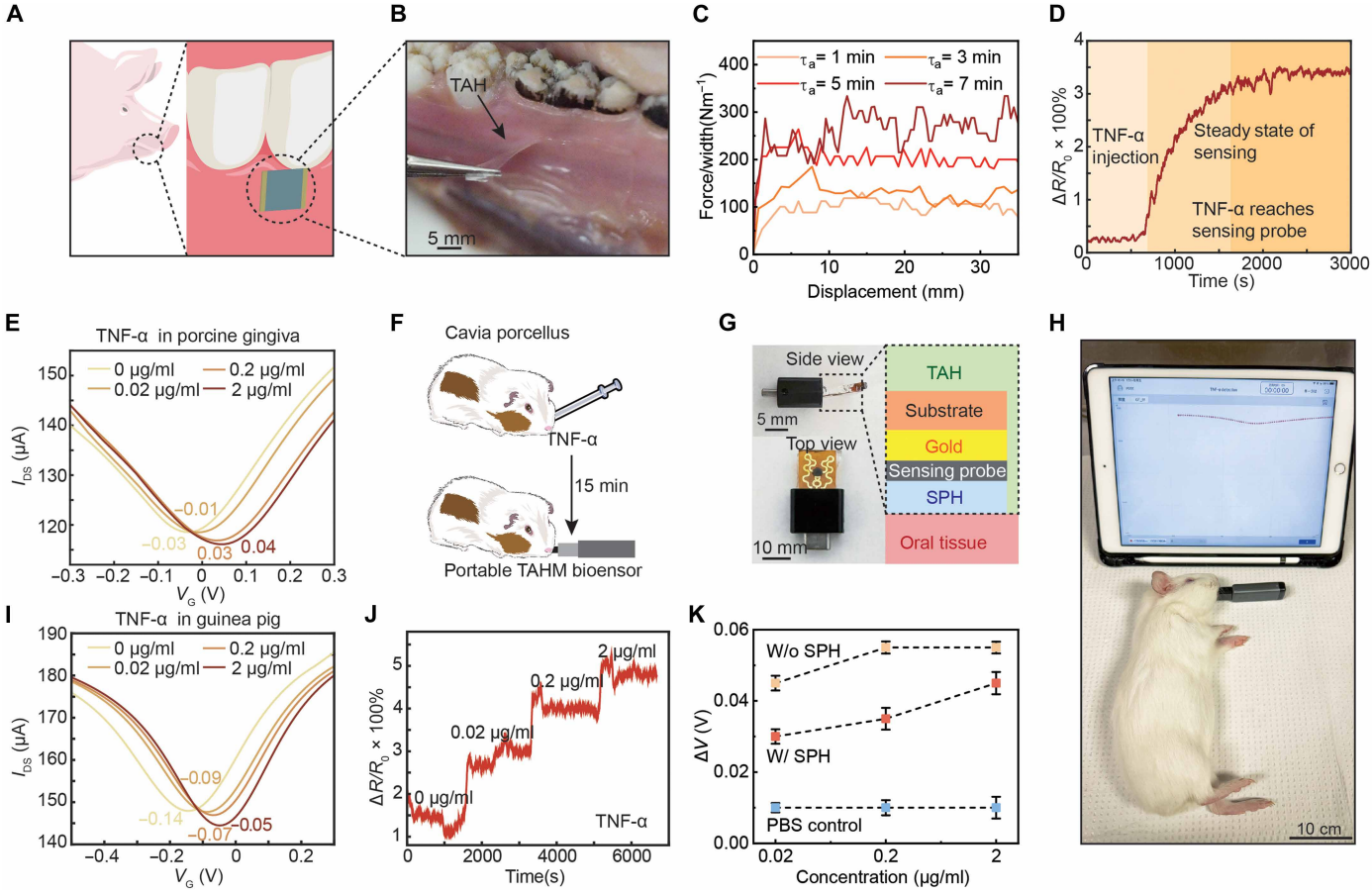

Fig. 5. Ex vivo and in vivo evaluations of the TAHM biosensor. (**A**) Schematic illustration of the TAHM biosensor adhered to porcine gingival tissue. (**B**) Optical image of a TAH patch attached to wet porcine gingiva. (**C**) Adhesion performance of the TAH patch at various adhesion times (τ_a) on wet porcine gingiva. (**D**) Real-time detection of TNF-α using a TAHM biosensor applied to porcine gingiva following local injection of human TNF-α solution. (**E**) Dirac point shifts corresponding to different TNF-α concentrations in the ex vitro model. (**F**) Schematic of the in vivo experiment using guinea pigs as the animal model. (**G**) Optical images of the TAHM biosensor connected to a portable adapter, and schematic of its structural configuration. (**H**) Optical image of the biosensor during in vivo testing. (**I**) Dirac point shifts correspond to different TNF-α concentrations in the in vivo model. (**J**) Real-time resistance changes of the TAHM biosensor in response to various TNF-α concentrations in the ex vivo model. (**K**) Comparison of signal output (voltage change) of biosensors with and without the SPH membrane and in PBS control in the ex vivo model. Scale bars, 5 mm [(B) and (G), top], 10 mm [(G), bottom], and 10 cm (H). Data in (K) represent mean ± SD ($n = 8$).

indicating sufficient adhesion strength under realistic conditions. These data indicate that the adhesion strength increases with prolonged adhesion time and gradually reaches a plateau within 5 min. Notably, when the dry TAH comes into contact with the moist tissue surface, it can achieve stable initial anchoring within ~5 s. This near-instantaneous adhesion is advantageous for clinical applications, enabling rapid and effective fixation in wet environments.

Next, we perform ex vivo characterization of our TAHM biosensor, by evaluating the sensing performance by injecting human TNF-α solution into the porcine gingival tissue using a 1-ml syringe and needle (0.3 ml at 0.2 μg/ml). Immediately following the injection, the TAHM biosensor is gently pressed onto the tissue surface for ~5 s to ensure stable contact, allowing for the monitoring of TNF-α diffusion from the inner tissue toward the sensing interface. Given the limited volume of emitted tissue exudate, we evaluate the signal output of the TAHM biosensor under varying sample volumes. The results show negligible variation between 20 and 40 μl (fig. S24). In addition, the hydrophilic nature of the SPH membrane promotes uniform spreading of the surface fluid, ensuring effective coverage of the electrode. Its diffusion time is estimated using the one-dimensional diffusion equation $t \approx L^2/(2D)$ (*71*) where $L = 130$ μm and $D = 3.73 \times 10^{-12}$ m^2s^{-1}, yielding an approximate diffusion time of 37 min. To ensure signal stability, we performed continuous measurements over 50 min. As shown in Fig. 5D, a distinct signal change is observed at ~11 min, indicating the arrival of TNF-α at the sensing surface. The signal continues to rise and reaches a plateau for around 27 min, reflecting the establishment of a local equilibrium in TNF-α concentration. The shortened reaction time can be attributed to mechanical deformation of the SPH membrane during attachment. This response latency is primarily governed by the diffusion time required for TNF-α to migrate from the injection site to the sensor interface. In practice, signal transduction initiates immediately upon TNF-α contact with the sensing patch. The response time can be further reduced by minimizing the thickness of the SPH membrane. When used in combination with the TAH patch, which enables near-instantaneous adhesion to wet tissue, the TAHM biosensor achieves rapid and stable attachment at the target site, enabling real-time, on-site molecular detection. This configuration is

well suited for practical biomedical applications. Furthermore, Fig. 5E shows a consistent rightward shift of the Dirac point with increasing TNF-α concentrations, confirming the biosensor's capability for quantitative detection in tissue environments and establishing a foundation for subsequent in vivo studies.

Next, we evaluate the in vivo sensing performance of the TAHM biosensor using guinea pigs as the animal model. As TNF-α expression in healthy guinea pigs remains low and does not exhibit substantial fluctuations, exogenous human TNF-α is injected into the gingival tissue of anesthetized guinea pigs to simulate an inflammatory environment, following the same protocol used in the porcine gingiva model. This setup enables the induction of a controlled increase in TNF-α concentration within a stable physiological environment, allowing the TAHM biosensor to effectively capture and monitor the dynamic changes in TNF-α levels in real time. After a 15-min stabilization period to allow diffusion and equilibration of TNF-α concentration, the TAHM biosensor is applied to the gingival surface for measurement (Fig. 5F). The biosensor used for in vivo testing consists of a graphene/MXene sensing probe integrated on a PI substrate, a selectively permeable hydrogel membrane, and a TAH patch, as schematically illustrated in Fig. 5G. A portable wireless adapter enables real-time transmission of sensing data to a graphical user interface, allowing continuous monitoring of Dirac point shifts during measurement (Fig. 5H). Figure 5I presents typical transfer curves recorded in an experiment conducted three times, showing a rightward shift in the Dirac point with increasing TNF-α concentration. These findings demonstrate that this sensor can accurately detect dose-dependent changes in TNF-α in the oral environment and can effectively output distinguishable signals while neglecting nontarget inhibitory factors in the oral cavity.

One unfavorable condition for quantitative detection of biomarkers from oral mucosa is associated with regional variations of the presence or absence of keratinized epithelium; nonkeratinized epithelial areas have high permeability, while keratinized areas, including the gingiva, have significantly lower permeability (*72*, *73*). Consequently, the amount of exudate and the biomarkers it contains from keratinized gingiva, but not from GCF, is extremely low; without proper isolation, exudate will be immediately diluted by saliva and eliminated from the oral cavity through physiological movements such as swallowing.

Despite these unfavorable conditions, our TAHM biosensor demonstrates the ability to detect TNF-α exuded from keratinized gingiva. Specifically, we collect tissue exudates from the gingival surface of guinea pigs following localized TNF-α injection to perform ex vivo characterizations. To enable real-time monitoring, we integrate the FET sensor with a circuit that continuously tracks changes in channel resistance, which indirectly reflects Dirac point shifts induced by TNF-α binding. As shown in Fig. 5J, this setup captures real-time resistance changes between the source and drain terminals under $V_g = 0$, enabling rapid, label-free detection of TNF-α concentration changes. Upon exposure to a higher concentration of TNF-α in the exudate, the channel resistance increases sharply within 5 s, demonstrating a rapid response time suitable for clinical applications. Last, we assess the effectiveness of the SPH membrane by comparing the sensor outputs from the collected exudate samples. As illustrated in Fig. 5K, in the absence of the SPH membrane, voltage responses do not exhibit a clear correlation with TNF-α concentration, where similar signal intensities are observed at both 0.2 and 2 μg/ml. In contrast, with the SPH membrane applied, the signal intensity exhibits a clear concentration-dependent increase, despite a slight reduction in absolute amplitude, indicating improved sensing specificity and performance.

In summary, our ex vivo characterizations demonstrate that regional variations in exudate can be mitigated by introducing SPH membrane, which isolates the measurement area and eliminate inhibitory factors via molecular sieving. In addition to its excellent performance, our device advances beyond most existing platforms that remain confined to in vitro settings. We are among the few to perform in vivo validation and, to our knowledge, the only study that compares detection accuracy between mixed and pure solutions (table S2). In future studies, we aim to broaden the range of detectable biomarkers beyond TNF-α by integrating target-specific antibodies and improving detection speed through the optimization of hydrogel properties. As a subsequent step, we intend to establish a disease-relevant model by administering lipopolysaccharide to induce oral inflammation (*74*), which will further support the translational potential of the biosensing platform.

DISCUSSION

According to the World Health Organization's ASSURED criteria, deployable POC devices should be sensitive, specific, affordable, user friendly, rapid and robust, equipment-free, and deliverable to end users. Currently, professional-grade quantitative POC devices that meet the ASSURED criteria have not been achieved in oral medicine. In this work, we present a robust and sensitive TAHM biosensor capable of stable in situ detection within the dynamic and wet environment of the oral cavity. The sensor integrates three key components: (i) a graphene/MXene-based sensing probe functionalized with a TNF-α–specific aptamer (VR11), (ii) an SPH membrane that filters out nontarget biomolecules, and (iii) a TAH patch that forms strong covalent bonds with both the wet tissue and sensor substrate. In addition, our TAHM biosensor can operate on a compact portable device for ease of use and rapid measurement. This integrated design addresses three major challenges in oral biosensing: insufficient sensitivity, ineffective selectivity, and inadequate fixation. Our TAHM biosensor demonstrates high sensitivity and interference-resistant performance, as validated through comprehensive in vitro, ex vivo, and in vivo characterizations. Collectively, these findings establish the feasibility of real time in situ monitoring of inflammatory cytokines in the oral cavity and underscore the sensor's potential for POC diagnostics and personalized healthcare. Looking ahead, we aim to evaluate its clinical efficacy through expanded trials further, advancing its integration into routine dental practice and broader community health monitoring platforms.

MATERIALS AND METHODS

All chemicals were purchased from Sigma-Aldrich unless otherwise specified and used as received without further purification. The synthesis of the TAH patch and the SPH membrane involved the following reagents: AAc-NHSester, AAc, AAm, *N*,*N*-methylenebisacrylamide (MBAA), and ammonium persulfate (APS). For silanization of the glass substrate, TMSPMA and acetic acid were used to prepare the silane bonding solution. For the flexible PI-based electrode, PI film (5 Mil, Kapton), poly(pyromellitic dianhydride-co-4,4′-oxydianiline), amic acid solution (liquid PI), photoresist gel (AZ 4620),

and its developer were prepared. For grafting amine groups on the PI substate, hexamethyldiamine (HMDA) was used to prepare the silane bonding solution. For the in vitro biocompatibility tests, RPMI 1640 medium (Life Technologies), fetal bovine serum, and penicillin-streptomycin (Life Technologies) were used. Porcine tissues and porcine jaw were obtained from Sierra for Medical Science (research-grade biological tissue supplier).

The fabrication of the MXene-based FETs used the following materials: Ti_3AlC_2 MAX phase powder (Jilin 11 Technology Co.), lithium fluoride (LiF), 1× PBS buffer, hydrochloric acid (HCl), GA (Thermo Fisher Scientific), poly(methyl methacrylate) (PMMA), copper etchant, and polydimethylsiloxane (PDMS). For surface functionalization of the TAHM biosensor, recombinant human TNF-α protein (R&D Systems) and purified VR11 single-stranded DNA aptamer (5′-NH_2-TGGTGGATGGCGCAGTCGGCGACAA-3′, Integrated DNA Technologies) were used. Simulated intestinal fluid, artificial saliva, and GCF were obtained from Biochemazone Inc. *Sm* was sourced from the American Type Culture Collection (ATCC), and the anti-*Sm* antibody was obtained from antibodies-online Inc. For *Sm* culturing, brain heart infusion (BHI) broth was used. To test the sensing specificity and diffusion in hydrogel membrane, we used human sAA and IL-6 (R&D Systems). For FRAP experiments, NHS-fluorescein (5/6-carboxyfluorescein succinimidyl ester, mixed isomers, Thermo Fisher Scientific) was used.

Synthesis of TAH patch and SPH membrane

Synthesis of the TAH patch

To prepare the TAH precursor, 3 ml of AAc, 0.1 g of AAc-NHS ester, and 2 g of AAm were dissolved in 10 ml of DI water using an ultrasonic cleaner (DK SONIC) for 20 min until complete dissolution of the AAc-NHS ester. Subsequently, 2 ml of 0.23 wt % MBAA and 200 μl of APS were added, and the mixture was thoroughly stirred and degassed for 30 s. Two quartz glass slides (75 mm by 50 mm by 1 mm) were treated with a water-repellent agent. Hollow parafilm spacers (~250 μm thick) were placed between the slides to define the hydrogel thickness. The final thickness of the hydrogel patch was controlled by varying the number of parafilm layers (*2*, *4*, *6*, *8*). Then, 2 ml of the hydrogel precursor was injected between the quartz slides with parafilm spacers and sealed using four clips on each side. The assembly was cured under ultraviolet (UV) light (365 nm, UVP CL-1000) for 120 min. After curing, one quartz slide was removed, and the hydrogel patch was allowed to air dry for 12 hours at room temperature. The dried hydrogels could be fabricated in advance and were sealed with desiccant and stored at −25°C until use (fig. S25A). The hydrogel detachment solution was prepared by dissolving 0.85 g of sodium bicarbonate and 3 g of glutathione in 10 ml of DI water (*62*), followed by stirring for 1 hour at room temperature. The solution was stored in a sealed container at room temperature for further use.

Synthesis of the SPH membrane

To synthesize the SPH membrane, 1.2 g of AAm, 1 ml of 0.23% MBAA, and 200 μl of APS were dissolved in 10 ml of DI water, thoroughly mixed, and degassed for 30 s. The cross-linking density of the SPH membrane was adjusted by varying the concentrations of AAm or MBAA. The precursor solution was then injected between two glass substrates with a hollow acrylic mold (1 mm thick) used as a spacer and secured with four clips on each side. This dimension was used for the subsequent FRAP experiments, whereas a thinner SPH layer of ~130 μm was used for the in vivo study, molded using a single layer of microscopic cover glass. The assembly was placed in an incubator (UVP CL-1000) and cured under UV light (365 nm) for 120 min. After curing, the SPH was trimmed to the desired size for preservation. The films were stored in sealed bags at room temperature until use; however, it is recommended to use them as soon as possible to minimize dehydration of the hydrogel (fig. S25B).

Synthesis of the TMSPMA silane solution

To prepare the glass-bonding silane solution, 200 μl of TMSPMA and 30 μl of acetic acid were added to 200 ml of DI water and stirred using a magnetic stirrer for 4 hours at room temperature until a clear solution was obtained. The resulting silane solution was sealed with parafilm and stored at room temperature for subsequent use.

Synthesis of the HMDA solution

To prepare the HMDA solution, 1 g of HMDA was fully dissolved in 10 ml of DI water. The HMDA solution was sealed with parafilm and stored at room temperature for subsequent use.

Fabrication of graphene/MXene sensing probe

Fabrication of monolayer graphene

Large-area monolayer graphene was synthesized via chemical vapor deposition on a copper foil (2 × 10 cm) and subsequently transferred onto a glass substrate, following a previously reported procedure (*75*). Specifically, a thin layer of PMMA was spin coated on the graphene surface, followed by baking at 130°C for 5 min. This PMMA/graphene/copper composite can be stored in a sealed bag at room temperature for subsequent use (fig. S25C).

Fabrication of Ti_3C_2-MXene

Ti_3C_2-MXene was prepared by selectively etching the aluminum layer from Ti_3AlC_2 (MAX phase) using a LiF/HCl-based etchant. Briefly, 0.8 g of LiF was added to 10 ml of 9 M HCl (prepared by diluting 12 M concentrated HCl) and stirred at room temperature for 30 min to generate an in situ hydrofluoric acid solution. Subsequently, 1 g of Ti_3AlC_2 powder was gradually added to the etching solution under continuous stirring at 35°C for 30 hours. The resulting suspension was centrifuged at 3500 rpm for 6 min, and the supernatant was discarded. The solid residue was washed repeatedly with DI water and centrifuged under the same conditions until the pH of the supernatant reached approximately 6. The collected precipitate was freeze dried for 48 hours to obtain multilayer Ti_3C_2-MXene powder (fig. S2). To prepare delaminated MXene nanosheets, the dried multilayer powder was redispersed in DI water and sonicated under an N_2 atmosphere for 2 hours to yield a homogeneous colloidal dispersion (fig. S25D). The overall thickness of the graphene/MXene ranged from ~1.2 to 4.5 nm. On the basis of our previous protocols (*21*, *75*), one to two layers of MXene (~1.36 nm per layer) were deposited onto the graphene surface (~1.02 nm thick).

Fabrication of gold electrode with PI substrate

The flexible Au electrode was fabricated via photolithography (*76*). A flexible PI film was first prepared, followed by spin coating a layer of liquid PI at 3000 rpm for 1 min. The film was then cured at 250°C for 1 hour. A ~50-nm gold layer was deposited onto the surface via sputtering. Subsequently, approximately 2 ml of photoresist was applied and spin coated for 30 s, followed by baking at 100°C for 10 min under a predesigned photomask (three electrodes, which function as the source, drain, and gate, respectively) and exposed in UV light for 10 s. It was then developed in a photoresist developer for 1 min until the pattern appeared. The gold was etched for ~1 min to reveal the desired pattern. Residual photoresist was removed by

rinsing with acetone, followed by isopropanol (IPA) and DI water. The electrodes were dried using nitrogen and stored for subsequent use (fig. S25E).

Surface functionalization of TNF-α sensor

Before each functionalization step, electrode surface was gently rinsed with DI water to remove residual reagents from the previous step. Subsequently, 30 μl of 25% (v/v) APTES solution was introduced into the chamber and allowed to react for 1 hour at room temperature, for subsequent grafting of GA and VR11. After rinsing, 20 μl of 15% (v/v) GA solution was added and incubated for an additional hour. Last, 20 μl of VR11 aptamer solution (0.16 mg/ml) was introduced into the chamber and incubated for 1 hour to allow covalent immobilization onto the functionalized surface. The surface functionalization of *Sm* sensor followed the same procedure as TNF-α sensor, except that the VR11 aptamer was replaced with an anti-*Sm* antibody (fig. S26A).

Assembly of TAHM biosensor

Fabrication of the glass substrate bonded on a TAH patch

A 170-μm-thick observation slide was first trimmed to an appropriate size and then incubated in a TMSPMA-based silane solution for 12 hours at room temperature, followed by drying under a nitrogen stream. Immersion in the TMSPMA solution introduced methacrylate functional groups onto the glass surface. The functionalized slide was then placed at the center of a water-repellent–treated glass substrate. The subsequent fabrication procedures were identical to those described in the "Synthesis of the TAH patch" section (fig. S11).

Fabrication of the G-MXene FET on a glass substrate for benchtop characterizations

PDMS prepolymer and curing agent were mixed at a 10:1 weight ratio and degassed under vacuum for 10 min. The mixture was then poured into a mold and cured at 45°C for 10 hours. After curing, the PDMS chamber was affixed to an as-prepared glass substrate coated with a monolayer graphene film using silicone adhesive, and the assembly was allowed to cure at room temperature for an additional 3 hours. The gate electrode consists of an external silver/silver chloride (Ag/AgCl) reference rod. Subsequently, 30 μl of ultrasonically treated MXene dispersion was added into the chamber and allowed to dry at room temperature for 4 hours. During this process, the MXene nanosheets adsorbed onto the graphene surface via electrostatic interactions, forming the sensing interface (fig. S26B). The subsequent functionalization procedures followed the protocol described in the "Surface functionalization of TNF-α sensor" section

Fabrication of the TAHM biosensor on a PI substrate for in vivo demonstration

The as-prepared PMMA/graphene/copper composite was first trimmed to an appropriate size covering only the source and drain electrodes and then immersed in a copper etchant to dissolve the copper substrate as described above. After completing etching, the PMMA/graphene film remained floating on the liquid surface. A plasma-treated electrode was subsequently immersed beneath the floating film and carefully lifted to retrieve the PMMA/graphene layer onto the sensing area. After drying, the composite became firmly laminated onto the electrode surface, covering only the drain and source regions, and allowed to dry completely. The electrode was then immersed in acetone for 1 hour to dissolve the PMMA layer, followed by sequential cleaning with IPA and DI water, as outlined previously. Next, MXene was directly deposited onto the exposed graphene region and allowed to dry completely. To functionalize the PI films with amine groups, the electrodes were cleaned with ethanol and DI water, dried under a nitrogen flow, and immersed in a 10% (w/w) HMDA aqueous solution for 24 hours at room temperature (*60*). The electrodes were then rinsed with DI water and dried under nitrogen for preservation. Subsequent surface modification steps followed the protocol described in the Surface functionalization of TNF-α sensor section. Last, an as-prepared SPH membrane was trimmed to approximately match the size of the functionalized area and gently attached to the sensing region. The electrode was lightly rinsed and then gently laminated onto an as-prepared dry TAH patch under mild compression to ensure conformal adhesion. Thus, a TAHM biosensor was successfully fabricated (fig. S26C).

Verification of the effective surface functionalization of TAHM biosensor

Verification by FTIR spectrometer

FTIR spectroscopy was performed using a Bruker LUMOS II spectrometer to verify the surface functionalization of the TAHM biosensor. Measurements were carried out in attenuated total reflectance mode with a spectral resolution of 4 cm^{-1} over the wave number range of 750 to 4000 cm^{-1}. The analyzed samples included pristine MXene, MXene functionalized with APTES (MXene/APTES), further modified with GA (MXene/APTES/GA), and lastly conjugated with the VR11 aptamer (MXene/APTES/GA/VR11). All samples were collected as freeze-dried powders following each reaction step.

Verification by FET

FET measurements were performed using a Keithley 4200-SCS Parameter. The gate voltage (V_g) was swept from −1 to +1.5 V with a step size of 0.01 V, while the drain-to-source voltage (V_{ds}) was held constant at 10 mV.

Verification by CV

CV measurements were conducted using a Gamry electrochemical workstation to evaluate the electrochemical properties of the functionalized sensor surface. Experiments were carried out in 1× PBS using a standard three-electrode configuration, in which the functionalized sensor served as the working electrode, a platinum wire as the counter electrode, and a Ag/AgCl (1 M KCl) electrode as the reference electrode. The potential window was scanned from −0.2 to +0.8 V at a scan rate of 100 mV/s.

Verification by SEM

SEM was performed using a JEOL JSM-7500F to examine surface morphology. Atomic force microscopy was conducted with a Bruker Dimension Icon system for nanoscale topographic imaging. X-ray photoelectron spectroscopy (XPS) was carried out using an Omicron XPS/UPS system to analyze elemental composition and chemical states. XRD measurements were conducted with a Bruker-AXS D8 Vario x-ray powder diffractometer to evaluate the crystalline structure of the samples.

In vitro sensing characterizations of TAHM biosensor

All sensing characterizations were conducted using a Keithley 4200-SCS parameter analyzer. Copper leads were soldered to silver-paste contacts at both ends of the graphene/MXene channel to serve as the drain and source electrodes. A PDMS chamber was used to confine the electrolyte above the sensing area, and a miniature Ag/AgCl electrode (StonyLab) immersed in the solution served as the gate electrode. Baseline transfer characteristics were recorded in 0.01× PBS, followed by identical measurements in artificial saliva, simulated intestinal fluid, and synthetic GCF to evaluate sensor performance

under physiologically relevant conditions. The sensing response was further characterized across a range of TNF-α concentrations and in heterogeneous fluids containing *Sm*, IL-6, and sAA to assess sensitivity and selectivity.

The LOD was determined according to the 3-sigma principle (*50*, *51*), where $C_{LOD} = 10^{\frac{(\Delta V_{blank} + 3\sigma - b)}{s}}$ where *S* and *b* are the slope and intercept of the calibration curve (fig. S28, A and B), respectively. ΔV_{blank} and σ are Dirac point shift and the SD of the blank signal (fig. S28, C and D), respectively. In the case without an SPH, $C_{LOD} = 10^{\frac{(0.042+3\times0.023-0.077)}{0.073}} = 2.9$ fg/ml. In the case with an SPH, $C_{LOD} = 10^{\frac{(0.011+3\times0.017-0.0267)}{0.028}} = 18.2$ fg/ml.

Fluorescence recovery after photobleaching

Sm culture and optical density measurement

Sm was revived from a lyophilized pellet according to the manufacturer's instructions. The pellet was rehydrated in 0.5 ml of sterile BHI broth and transferred aseptically into 5 ml of fresh BHI broth (primary culture). Following incubation at 37°C for 24– to 48 hours, 0.5 ml of the primary culture was used to inoculate another 5 ml of fresh BHI broth (secondary culture), which was incubated at 37°C for 12 to 18 hours until visible turbidity developed. Bacterial concentration was determined by measuring optical density at 600 nm (OD_{600}) using a UV-visible spectrophotometer. Cultures were gently mixed and diluted in sterile PBS to obtain OD_{600} values within the linear range (0.1 to 0.8). The absorbance was then converted to CFU concentration based on a preestablished OD_{600}-CFU calibration curve, where an OD_{600} of 1.0 corresponds to ~1×10^8 CFU ml^{-1} for *Sm* (*77*).

Labeling of biomolecules with NHS-fluorescein

TNF-α, IL-6, sAA, and *Sm* were labeled with NHS-fluorescein via amine-reactive conjugation, leveraging the presence of surface-exposed amine groups. To prepare the labeling solution, 1 mg of NHS-fluorescein was dissolved in 100 μl of dimethyl sulfoxide and 15 ml of DI water and mixed with 1 ml of TNF-α solution (1000 fg/ml), 1 ml of IL-6 solution (1000 fg/ml), 1 ml of sAA (1 U/ml), and *Sm* (0.25×10^8 CFU/ml). The mixture was stirred at 50 rpm for 3 hours at room temperature and protected from light using aluminum foil. The reaction mixture was evenly distributed into four centrifugal filter tubes (4-ml capacity and 10-kDa molecular weight cutoff; 4-ml capacity and 30-kDa molecular weight cutoff for *Sm* only) and centrifuged at 4000 rpm for 10 min at room temperature. Each tube was then refilled with 4 ml of DI water and centrifuged again. This washing step was repeated three times to remove unreacted fluorophore. The labeled product was protected from light and stored at −25°C for subsequent use (fig. S5).

Preparation of hydrogel samples for FRAP analysis

After thawing the NHS-fluorescein–labeled TNF-α, 1 ml of DI water was added to the centrifugal filter tube and vortexed for 1 min. Then, 100 μl of the resulting solution was mixed with 1 ml of the hydrogel precursor prepared according to the protocol described in the "Synthesis of the SPH membrane" section. The mixture was degassed for 30 s and injected into a small acrylic mold. The mold was covered with aluminum foil to protect from light and placed on a hot plate at 60°C for 1 hour to allow complete curing. The cured hydrogel containing fluorescently labeled TNF-α was stored at −25°C until further use. The preparation of hydrogel samples containing *Sm* followed the same procedure, with NHS-fluorescein–labeled TNF-α replaced by NHS-fluorescein–labeled *Sm*.

FRAP experiment

FRAP measurements were performed using a confocal laser scanning microscope equipped with a 20× objective and a 488-nm laser (10 mW). An SPH sample containing NHS-fluorescein–labeled TNF-α (10 mm by 10 mm by 1 mm) was mounted on the microscope stage. A circular region (24 μm in diameter) at the center of the hydrogel was photobleached by focusing the laser at full power for 4 s. Fluorescence recovery was monitored at 1-s intervals for 100 s using the 488-nm scanning laser operated at 0.5% of its maximum power. The same protocol was applied to *Sm* labeled with NHS-fluorescein, replacing the TNF-α hydrogel with a hydrogel sample containing the labeled bacteria. System calibration was performed before imaging to ensure optimal resolution and focus.

Mechanical characterizations of the TAH patch

Adhesion characterization of the porcine skin and the glass substrate adhered to the TAH

All mechanical tests were performed using a UStretch testing device (CellScale). To evaluate the adhesive performance of the TAH patch between wet biological tissue and a glass substrate, porcine skin was used. The skin samples were thoroughly cleaned with ethanol and DI water, cut into 2 cm–by–8 cm pieces, and affixed to a plastic film of the same dimensions to provide structural support. The prepared porcine skin was then placed onto a quartz glass substrate coated with a dried TAH patch (50 mm by 10 mm), and a gentle compressive force (~5 kPa) was applied for ~5 s to ensure conformal contact. This assembly (porcine skin/TAH/Glass) was then left at ambient conditions for a controlled adhesion time τ_a before performing adhesion characterization. Interfacial toughness between the tissue and substrate was quantified via a 90° peeling test, following the ASTM D6862 standard. The extended portion of the porcine skin was clamped by the vertical arm of the UStretch device, while the quartz glass substrate was fixed to a horizontal movable stage using clips. During testing, the porcine skin was pulled vertically at a constant speed of 1 mm/s, while the horizontal stage was simultaneously moved at the same speed to maintain a constant 90° peeling angle throughout the process. To evaluate adhesion on porcine gingiva, hydrogel patches backed with a stiff plastic layer were applied to porcine gingival tissue, and the same 90° peeling protocol was followed. The interfacial toughness was calculated by dividing the steady-state peeling force by the width of the TAH patch (10 mm). To evaluate the effect of different preloading pressures on adhesion strength, a uniform downward pressure was applied using the same testing apparatus during the attachment of the TAH to porcine skin. For assessing the influence of swelling, the adhered TAH–porcine skin assemblies were fully immersed in DI water for designated time periods. Subsequently, 90° peeling tests were performed to quantify changes in adhesion performance.

Bulk characterization of the TAH patch

For the uniaxial stretching test, a large, dried TAH film was trimmed into dimensions of 3 cm by 2 cm. Both ends of the hydrogel film were glued between two 3 cm–by–2 cm acrylic pieces, with 1 cm–by–0.5 cm acrylic pieces attached at the ends as holders, leaving a 1-cm height of the TAH exposed for stretching. The assembled structure was then immersed in a DI water tank for rehydration, with the hydration time controlled. After measuring its thickness

following rehydration, the hydrogel sample was clipped onto the UStretch testing device and stretched vertically at a rate of 1 mm/s until failure occurred. For notched hydrogel samples, the same procedure was followed, but before stretching, a 1-cm notch was introduced at the center of the hydrogel. To measure mechanical hysteresis, the TAH was retracted at the same rate after being stretched to a controlled stretch ratio (λ). Fracture toughness was determined using experimental data from both notched and unnotched samples, while Young's modulus was calculated from the initial slope of the stress-stretch curve of the unnotched samples.

Characterization of the strain insensitivity of the TAHM biosensor

To evaluate the influence of mechanical deformation on the TAHM biosensor, a sensor (20 mm by 20 mm) was centrally affixed onto a dried TAH patch (75 mm by 50 mm). The two ends of the hydrogel were bonded between two acrylic plates (50 mm by 20 mm), with additional acrylic holders (10 mm by 5 mm) attached at both ends to facilitate gripping. This configuration exposed a 40-mm-high region of hydrogel for tensile loading. The assembled construct was immersed in a DI water bath for 10 min, ensuring that only the hydrogel film was submerged. After rehydration, the construct was mounted on a UStretch testing device, and conductive adhesive tapes were applied to the sensor's contact pads. Electrical signals were monitored using a Keithley DAQ6510 data acquisition system, which continuously recorded resistance changes during mechanical deformation. To investigate the sensor's strain response, three key parameters were systematically varied: stretch magnitude, stretching frequency, and number of cycles. Corresponding resistance variations were recorded in real-time under each condition. To further assess biosensing performance under strain, 10 μl of TNF-α solution (1000 fg/ml) was dispensed onto the sensing area. After a 30-min incubation to allow signal stabilization, uniaxial stretching was applied using the UStretch system, and changes in electrical resistance were recorded for both TNF-α–treated and untreated conditions.

In vitro biocompatibility tests

In vitro biocompatibility assays were performed for both TAH and SPH. BT549 epithelial cells were cultured in complete growth medium consisting of RPMI 1640 medium, supplemented with 10% fetal bovine serum and 1% penicillin-streptomycin. To prepare the conditioned medium, individual hydrogel samples (~1 cm by 1 cm by 120 μm) were incubated in 2 ml of complete medium at 37°C for 24 hours. Pristine complete medium without hydrogel incubation served as the control. BT549 cells were seeded into 96-well plates and incubated at 37°C with 5% CO_2 for 48 hours. Cell viability was assessed using the LIVE/DEAD Viability/Cytotoxicity Kit (Life Technologies), following the manufacturer's instructions. The assay used 4 μM calcein-AM to stain viable cells and ethidium homodimer-1 to label nonviable cells. Fluorescence imaging was performed using a Leica SP8 confocal microscope. Live cells were visualized at 495-nm excitation/515-nm emission, while dead cells were detected at 495-nm excitation/635-nm emission.

Ex vivo and in vivo sensing characterizations of TAHM biosensor

Ex vivo characterization of adhesion performance

A porcine jaw was used to evaluate the adhesion performance of the TAH patch on gingival tissue. The jaw was thoroughly cleaned with ethanol and DI water to remove surface contaminants. A TAH was then applied to the gingival region and left undisturbed for a predefined adhesion time (τ_a). To facilitate mechanical testing, a thin plastic film was bonded to the backside of the hydrogel patch to serve as a stiff backing. For the 90° peeling test, the porcine jaw was fixed onto a sliding rail with the gingival surface facing upward. The subsequent adhesion measurement followed the same protocol described in the "Adhesion characterization of the porcine skin and the glass substrate adhered to the TAH" section.

Ex vivo characterization of sensing performance

Human TNF-α solution (0.2 μg/ml in sterile saline) was injected into the submucosal layer of porcine gingival tissue. A total volume of 0.5 ml was delivered using a 1-ml syringe equipped with a standard needle. The injection was performed slowly to a depth of ~2 to 3 mm to ensure uniform distribution within the tissue. Immediately following the injection, a TAHM biosensor (sensing area: 10 mm by 10 mm and sensor dimension: 20 mm by 20 mm by 0.5 mm) was gently applied to the gingival surface, with the SPH membrane in direct contact with the tissue. The biosensor was held in place under ambient conditions without external loading to ensure conformal contact between the sensor and the wet tissue. The setup was maintained undisturbed at room temperature to allow diffusion of TNF-α from the submucosal region to the sensor interface. Real-time monitoring of the biosensor's electrical signal was conducted using an LCR meter configured to continuously record changes in channel resistance.

In vivo characterization

Adult guinea pigs (*Cavia porcellus*; $n = 2$, 300 to 400 g) were housed under controlled environmental conditions (22° ± 1°C, 50% relative humidity, and 12-hour light/dark cycle) with ad libitum access to food and water. Before testing, animals were anesthetized via intramuscular injection of ketamine (50 mg/kg) and xylazine (5 mg/kg) into the thigh muscle. TNF-α solutions (20, 200, and 2000 ng/ml in 0.9% sterile saline) were sequentially administered into the gingival sulcus (100 μl per concentration) using a microsyringe. A 15-min interval was maintained between each injection to allow sufficient TNF-α diffusion and prevent concentration overlapping. For in vivo measurements, TAHM biosensors were fabricated on PI substrates with gold electrodes and fully functionalized following protocols described previously (*13*). The biosensor was gently inserted into the oral cavity and positioned against the upper palatal mucosa with the SPH layer contacting the tissue. Gentle manual pressure was applied for ~5 s to ensure stable adhesion via the TAH layer. Real-time resistance measurements were recorded using a portable sensing module (sampling rate: 100 Hz). Upon completion, the sensor was removed by applying ~1 ml of detachment solution to the hydrogel-tissue interface. Animals were monitored until full recovery from anesthesia and subsequently returned to their standard housing environment (movie S3).

During in vivo characterization, tissue exudates were collected from the gingival sulcus of anesthetized guinea pigs following the local administration of TNF-α solutions at varying concentrations. After each injection, animals were left undisturbed for 15 min to allow adequate diffusion and establishment of localized TNF-α levels. Tissue exudates were then gently aspirated from the gingival site using a micropipette and immediately transferred for storage. A volume of 10 μl of TNF-α–containing exudate was drop cast directly onto the sensing region of a TAHM biosensor. Real-time electrical response was monitored by recording changes in channel resistance using an LCR meter, with continuous data acquisition for up to 2000 s following sample application.

Ethics approval

Animal tests at Texas A&M University were approved by the Institutional Animal Care and Use Committee (IACUC) (approval number: IACUC 2024-0148 M, expiration date: 29 August 2027) and followed ARRIVE guidelines.

Supplementary Materials

The PDF file includes:

Supplementary Text
Figs. S1 to S28
Tables S1 and S2
Legends for movies S1 to S3

Other Supplementary Material for this manuscript includes the following:

Movies S1 to S3

REFERENCES

1. H. Sasaki, K. Hirai, C. M. Martins, H. Furusho, R. Battaglino, K. Hashimoto, Interrelationship between periapical lesion and systemic metabolic disorders. *Curr. Pharm. Des.* **22**, 2204–2215 (2016).
2. M. Martínez-García, E. Hernández-Lemus, Periodontal inflammation and systemic diseases: An overview. *Front. Physiol.* **12**, 709438 (2021).
3. J. E. Allen, T. A. Wynn, Evolution of Th2 immunity: A rapid repair response to tissue destructive pathogens. *PLOS Pathog.* **7**, e1002003 (2011).
4. X. Hu, L. B. Ivashkiv, Cross-regulation of signaling pathways by interferon-γ: Implications for immune responses and autoimmune diseases. *Immunity* **31**, 539–550 (2009).
5. A. Al-Majid, S. Alassiri, N. Rathnayake, T. Tervahartiala, D.-R. Gieselmann, T. Sorsa, Matrix metalloproteinase-8 as an inflammatory and prevention biomarker in periodontal and peri-implant diseases. *Int. J. Dent.* **2018**, 7891323 (2018).
6. R. L. Muir, Peripheral arterial disease: Pathophysiology, risk factors, diagnosis, treatment, and prevention. *J. Vasc. Nurs.* **27**, 26–30 (2009).
7. I. Rotstein, J. H. S. Simon, Diagnosis, prognosis and decision-making in the treatment of combined periodontal-endodontic lesions. *Periodontol. 2000* **34**, 165–203 (2004).
8. J. D. Bader, D. A. Shugars, A. J. Bonito, Systematic reviews of selected dental caries diagnostic and management methods. *J. Dent. Educ.* **65**, 960–968 (2001).
9. M. Boccellino, A. De Rosa, M. Di Domenico, An ELISA test able to predict the development of oral cancer: The significance of the interplay between steroid receptors and the EGF receptor for early diagnosis. *Diagnostics* **13**, 2001 (2023).
10. D. Malamud, Oral diagnostic testing for detecting human immunodeficiency virus-1 antibodies: A technology whose time has come. *Am. J. Med.* **102**, 9–14 (1997).
11. C. Moonla, D. H. Lee, D. Rokaya, N. Rasitanon, G. Kathayat, W.-Y. Lee, J. Kim, I. Jeerapan, Review—Lab-in-a-mouth and advanced point-of-care sensing systems: Detecting bioinformation from the oral cavity and saliva. *ECS Sens. Plus* **1**, 021603 (2022).
12. S. Agrawal, S. Taneja, D. Shetty, V. Gopikrishna, V. K. Bhalla, Evaluating the concentration of MMP-9 and TNF-α in pulpal blood at various stages of pulpal inflammation in diabetics: A cross sectional study. *Eur. Endod. J.* **8**, 286–292 (2023).
13. T. H. Wong, J. Liu, Y. Cheng, Y. Xie, C. Anway, R. Lu, C. Ye, Z. Yu, Y. Wang, X. Liu, S. Lin, Electrical tissue adhesives for strain-insensitive in-situ biosensing. *Adv. Intell. Syst.* **7**, 2400697 (2024).
14. A. S. Cole, J. E. Eastoe, *Biochemistry and Oral Biology* (Butterworth-Heinemann, 2014).
15. V. Kesler, B. Murmann, H. T. Soh, Going beyond the Debye length: Overcoming charge screening limitations in next-generation bioelectronic sensors. *ACS Nano* **14**, 16194–16201 (2020).
16. D. W. Kimmel, G. LeBlanc, M. E. Meschievitz, D. E. Cliffel, Electrochemical sensors and biosensors. *Anal. Chem.* **84**, 685–707 (2012).
17. U. Chadha, P. Bhardwaj, R. Agarwal, P. Rawat, R. Agarwal, I. Gupta, M. Panjwani, S. Singh, C. Ahuja, S. K. Selvaraj, Recent progress and growth in biosensors technology: A critical review. *J. Ind. Eng. Chem.* **109**, 21–51 (2022).
18. A. K. Geim, Graphene: Status and prospects. *Science* **324**, 1530–1534 (2009).
19. Z. Ling, C. E. Ren, M.-Q. Zhao, J. Yang, J. M. Giammarco, J. Qiu, M. W. Barsoum, Y. Gogotsi, Flexible and conductive MXene films and nanocomposites with high capacitance. *Proc. Natl. Acad. Sci. U.S.A.* **111**, 16676–16681 (2014).
20. M. Hu, T. Hu, Z. Li, Y. Yang, R. Cheng, J. Yang, C. Cui, X. Wang, Surface functional groups and interlayer water determine the electrochemical capacitance of Ti_3C_2 T_x MXene. *ACS Nano* **12**, 3578–3586 (2018).
21. J. Li, Y. Zhang, C. Wei, Y. Li, Z. Peng, H.-Y. Chuang, L. Pearce, A. Boon, Y.-W. Huang, D. Kim, Advanced detection of SARS-CoV-2 and omicron variants via MXene-graphene hybrid biosensors utilizing nucleic acid probes. *ACS Appl. Nano Mater.* **7**, 28255–28272 (2024).
22. H. Nam, B.-R. Oh, P. Chen, M. Chen, S. Wi, W. Wan, K. Kurabayashi, X. Liang, Multiple MoS_2 transistors for sensing molecule interaction kinetics. *Sci. Rep.* **5**, 10546 (2015).
23. B. Ryu, H. Nam, B.-R. Oh, Y. Song, P. Chen, Y. Park, W. Wan, K. Kurabayashi, X. Liang, Cyclewise operation of printed MoS_2 transistor biosensors for rapid biomolecule quantification at femtomolar levels. *ACS Sens.* **2**, 274–281 (2017).
24. Y. Park, B. Ryu, B.-R. Oh, Y. Song, X. Liang, K. Kurabayashi, Biotunable nanoplasmonic filter on few-layer MoS_2 for rapid and highly sensitive cytokine optoelectronic immunosensing. *ACS Nano* **11**, 5697–5705 (2017).
25. J. Sun, L. Zhou, Z. Li, G. He, H. Mao, J. Zhao, J. A. Hunt, X. Chen, Perovskite-graphene heterostructure biosensor integrated with biotunable nanoplasmonic ternary logic gate for ultrasensitive cytokine detection. *Adv. Sci.* **12**, e03124 (2025).
26. D. Li, Y. Ren, R. Chen, H. Wu, S. Zhuang, M. Zhang, Label-free MXene-assisted field effect transistor for the determination of IL-6 in patients with kidney transplantation infection. *Mikrochim. Acta* **190**, 284 (2023).
27. D. Rani, Y. Singh, M. Salker, X. T. Vu, S. Ingebrandt, V. Pachauri, Point-of-care-ready nanoscale ISFET arrays for sub-picomolar detection of cytokines in cell cultures. *Anal. Bioanal. Chem.* **412**, 6777–6788 (2020).
28. N. Chen, H. Yang, Q. Li, L. Song, S. C. Gopinath, D. Wu, An interdigitated aptasensor to detect interleukin-6 for diagnosing rheumatoid arthritis in serum. *Biotechnol. Appl. Biochem.* **68**, 1479–1485 (2021).
29. M. T. Amen, T. T. T. Pham, E. Cheah, D. P. Tran, B. Thierry, Metal-oxide FET biosensor for point-of-care testing: Overview and perspective. *Molecules* **27**, 7952 (2022).
30. J. Xu, H. Lee, Anti-biofouling strategies for long-term continuous use of implantable biosensors. *Chem* **8**, 66 (2020).
31. M. J. Russo, M. Han, P. E. Desroches, C. S. Manasa, J. Dennaoui, A. F. Quigley, R. M. Kapsa, S. E. Moulton, R. M. Guijt, G. W. Greene, Antifouling strategies for electrochemical biosensing: Mechanisms and performance toward point of care based diagnostic applications. *ACS Sens.* **6**, 1482–1507 (2021).
32. N. Wisniewski, M. Reichert, Methods for reducing biosensor membrane biofouling. *Colloids Surf. B Biointerfaces* **18**, 197–219 (2000).
33. P.-H. Lin, B.-R. Li, Antifouling strategies in advanced electrochemical sensors and biosensors. *Analyst* **145**, 1110–1120 (2020).
34. N. Liu, Z. Xu, A. Morrin, X. Luo, Low fouling strategies for electrochemical biosensors targeting disease biomarkers. *Anal. Methods* **11**, 702–711 (2019).
35. A. Gong, X. Ma, L. Xiang, W. Ren, Z. Shen, A. Wu, Improved double emulsion technology for fabricating autofluorescent microcapsules as novel ultrasonic/fluorescent dual-modality contrast agents. *Colloids Surf. B Biointerfaces* **116**, 561–567 (2014).
36. L. Olde Damink, P. Dijkstra, M. Van Luyn, P. Van Wachem, P. Nieuwenhuis, J. Feijen, Glutaraldehyde as a crosslinking agent for collagen-based biomaterials. *J. Mater. Sci.* **6**, 460–472 (1995).
37. W. Safar, A. Azziz, M. Edely, M. Lamy de la Chapelle, Conventional Raman, SERS and TERS studies of DNA compounds. *Chem* **11**, 399 (2023).
38. Z. Hao, Z. Wang, Y. Li, Y. Zhu, X. Wang, C. G. De Moraes, Y. Pan, X. Zhao, Q. Lin, Measurement of cytokine biomarkers using an aptamer-based affinity graphene nanosensor on a flexible substrate toward wearable applications. *Nanoscale* **10**, 21681–21688 (2018).
39. N. Nakatsuka, K.-A. Yang, J. M. Abendroth, K. M. Cheung, X. Xu, H. Yang, C. Zhao, B. Zhu, Y. S. Rim, Y. Yang, Aptamer–field-effect transistors overcome Debye length limitations for small-molecule sensing. *Science* **362**, 319–324 (2018).
40. T. Chen, W.-H. Yu, J. Izard, O. V. Baranova, A. Lakshmanan, F. E. Dewhirst, The Human Oral Microbiome Database: A web accessible resource for investigating oral microbe taxonomic and genomic information. *Database* **2010**, baq013 (2010).
41. N. Ramasubbu, V. Paloth, Y. Luo, G. D. Brayer, M. J. Levine, Structure of human salivary α-amylase at 1.6 Å resolution: Implications for its role in the oral cavity. *Acta Crystallogr. D Biol. Crystallogr.* **52**, 435–446 (1996).
42. H. Daub, L. Traxler, F. Ismajli, B. Groitl, A. Itzen, U. Rant, The trimer to monomer transition of tumor necrosis factor-alpha is a dynamic process that is significantly altered by therapeutic antibodies. *Sci. Rep.* **10**, 9265 (2020).
43. M. Johnson, J. Bozzola, I. Shechmeister, Morphological study of *Streptococcus mutans* and two extracellular polysaccharide mutants. *J. Bacteriol.* **118**, 304–311 (1974).
44. J. A. Lemos, S. R. Palmer, L. Zeng, Z. T. Wen, J. K. Kajfasz, I. A. Freires, J. Abranches, L. J. Brady, The biology of *Streptococcus mutans*. *Microbiol. Spectr.* **7**, doi: 10.1128/microbiolspec.GPP3-0051-2018 (2019).
45. M. Kang, C. A. Day, A. K. Kenworthy, E. DiBenedetto, Simplified equation to extract diffusion coefficients from confocal FRAP data. *Traffic* **13**, 1589–1600 (2012).
46. M. Rubinstein, R. H. Colby, *Polymer Physics* (Oxford Univ. Press, 2003).
47. J. Liu, S. Lin, Strain-engineered particle diffusion in uniaxially deformed polymer networks. *J. Mech. Phys. Solids* **191**, 105732 (2024).
48. C. Ye, C. Wei, J. Liu, T. H. Wong, X. Liu, Z. Song, C. Wu, Z. Li, S. Lin, Mechano-diffusion of particles in stretchable hydrogels. *Soft Matter* **21**, 2230–2241 (2025).
49. J. C. Yang, S. J. Lim, C. H. Cho, D. Hazarika, J. P. Park, J. Park, Determination of tumor necrosis factor-α in serum using extended-gate field-effect transistor-based

chemosensors with molecularly imprinted polymer-coated gold dendrites. *Sens. Actuators B Chem.* **390**, 133982 (2023).
50. J. Ouyang, Y. Li, F. Yang, X. Wu, Z. Qiu, J. Shu, Electrochemical and field effect transistor dual-mode biosensor chip for label-free detection of cytokine storm biomarker with high sensitivity within a wide range. *Adv. Funct. Mater.* **34**, 2405212 (2024).
51. C. Huang, D. Li, J. Liu, S. Hou, W. Yang, H. Wang, J. Wang, Z. Wang, F. Li, Z. Hao, A flexible aptameric graphene field-effect nanosensor capable of automatic liquid collection/filtering for cytokine storm biomarker monitoring in undiluted sweat. *Adv. Funct. Mater.* **34**, 2309447 (2024).
52. Z. Wang, W. Dai, Z. Zhang, H. Wang, Aptamer-based graphene field-effect transistor biosensor for cytokine detection in undiluted physiological media for cervical carcinoma diagnosis. *Biosensors* **15**, 138 (2025).
53. C. Huang, W. Yang, H. Wang, S. Huang, S. Gao, D. Li, J. Liu, S. Hou, W. Feng, Z. Wang, Flexible/regenerative nanosensor with automatic sweat collection for cytokine storm biomarker detection. *ACS Nano* **18**, 21198–21210 (2024).
54. R. T. Arwani, S. C. L. Tan, A. Sundarapandi, W. P. Goh, Y. Liu, F. Y. Leong, W. Yang, X. T. Zheng, Y. Yu, C. Jiang, Stretchable ionic–electronic bilayer hydrogel electronics enable in situ detection of solid-state epidermal biomarkers. *Nat. Mater.* **23**, 1115–1122 (2024).
55. S. Li, J. Dai, M. Zhu, N. Arroyo-Currás, H. Li, Y. Wang, Q. Wang, X. Lou, T. E. Kippin, S. Wang, Implantable hydrogel-protective DNA aptamer-based sensor supports accurate, continuous electrochemical analysis of drugs at multiple sites in living rats. *ACS Nano* **17**, 18525–18538 (2023).
56. A. G. Nejad, C. D. Flynn, A. Geraili, S. Mirzaie, F. Esmaeili, H. Zargartalebi, S. Ahmed, V. B. Juska, J. Das, A. Abdrabou, Y. Y. Zhang, E. H. Sargent, S. O. Kelley, Continuous insulin monitoring using an antibody-protecting zwitterionic microneedle patch. *Nat. Biomed. Eng.*, doi: 10.1038/s41551-025-01477-7 (2025).
57. X. Xie, J. C. Doloff, V. Yesilyurt, A. Sadraei, J. J. McGarrigle, M. Omami, O. Veiseh, S. Farah, D. Isa, S. Ghani, Reduction of measurement noise in a continuous glucose monitor by coating the sensor with a zwitterionic polymer. *Nat. Biomed. Eng.* **2**, 894–906 (2018).
58. Y. Li, Z. Peng, N. J. Holl, M. R. Hassan, J. M. Pappas, C. Wei, O. H. Izadi, Y. Wang, X. Dong, C. Wang, MXene–graphene field-effect transistor sensing of influenza virus and SARS-CoV-2. *ACS Omega* **6**, 6643–6653 (2021).
59. H. Yuk, T. Zhang, S. Lin, G. A. Parada, X. Zhao, Tough bonding of hydrogels to diverse non-porous surfaces. *Nat. Mater.* **15**, 190–196 (2016).
60. H. Yuk, C. E. Varela, C. S. Nabzdyk, X. Mao, R. F. Padera, E. T. Roche, X. Zhao, Dry double-sided tape for adhesion of wet tissues and devices. *Nature* **575**, 169–174 (2019).
61. M. J. Fischer, "Amine coupling through EDC/NHS: A practical approach," in *Surface Plasmon Resonance: Methods and Protocols* (Springer, 2010), pp. 55–73.
62. X. Chen, H. Yuk, J. Wu, C. S. Nabzdyk, X. Zhao, Instant tough bioadhesive with triggerable benign detachment. *Proc. Natl. Acad. Sci. U.S.A.* **117**, 15497–15503 (2020).
63. T. Zhang, S. Lin, H. Yuk, X. Zhao, Predicting fracture energies and crack-tip fields of soft tough materials. *Extreme Mech. Lett.* **4**, 1–8 (2015).
64. S. Lin, C. D. Londono, D. Zheng, X. Zhao, An extreme toughening mechanism for soft materials. *Soft Matter* **18**, 5742–5749 (2022).
65. J. Yang, W. Illeperuma, Z. Suo, Inelasticity increases the critical strain for the onset of creases on hydrogels. *Extreme Mech. Lett.* **40**, 100966 (2020).
66. I. Lamster, R. D. Mandella, S. Zove, D. Harper, The polyamines putrescine, spermidine and spermine in human gingival crevicular fluid. *Arch. Oral Biol.* **32**, 329–333 (1987).
67. S. Goktas, J. J. Dmytryk, P. S. McFetridge, Biomechanical behavior of oral soft tissues. *J. Periodontol.* **82**, 1178–1186 (2011).
68. G. Theocharidis, H. Yuk, H. Roh, L. Wang, I. Mezghani, J. Wu, A. Kafanas, M. Contreras, B. Sumpio, Z. Li, A strain-programmed patch for the healing of diabetic wounds. *Nat. Biomed. Eng.* **6**, 1118–1133 (2022).
69. J. Li, A. D. Celiz, J. Yang, Q. Yang, I. Wamala, W. Whyte, B. R. Seo, N. Vasilyev, J. J. Vlassak, Z. Suo, Tough adhesives for diverse wet surfaces. *Science* **357**, 378–381 (2017).
70. Z. Yang, Z. Ma, S. Liu, J. Li, Tissue adhesion with tough hydrogels: Experiments and modeling. *Mech. Mater.* **157**, 103800 (2021).
71. P. Müller, A. F. Schier, Extracellular movement of signaling molecules. *Dev. Cell* **21**, 145–158 (2011).
72. C. A. Squier, B. K. Hall, The permeability of skin and oral mucosa to water and horseradish peroxidase as related to the thickness of the permeability barrier. *J. Invest. Dermatol.* **84**, 176–179 (1985).
73. C. Squier, The permeability of oral mucosa. *Crit. Rev. Oral Biol. Med.* **2**, 13–32 (1991).
74. B. Töllner, J. Roth, B. Störr, D. Martin, K. Voigt, E. Zeisberger, The role of tumor necrosis factor (TNF) in the febrile and metabolic responses of rats to intraperitoneal injection of a high dose of lipopolysaccharide. *Pflugers Arch.* **440**, 925–932 (2000).
75. J. Li, J. Liu, C. Wei, X. Liu, S. Lin, C. Wu, Hydrogel-gated MXene-graphene field-effect transistor for selective detection and screening of SARS-CoV-2 and *E. coli* bacteria. *ACS Appl. Mater. Interfaces* **17**, 2871–2883 (2025).
76. T. H. Wong, Y. Liu, J. Li, K. Yao, S. Liu, C. K. Yiu, X. Huang, M. Wu, W. Park, J. Zhou, Triboelectric nanogenerator tattoos enabled by epidermal electronic technologies. *Adv. Funct. Mater.* **32**, 2111269 (2022).
77. M. Gu, J.-H. Cho, J.-W. Suh, J. Cheng, Potential oral probiotic *Lactobacillus pentosus* MJM60383 inhibits *Streptococcus mutans* biofilm formation by inhibiting sucrose decomposition. *J. Oral Microbiol.* **15**, 2161179 (2023).

Acknowledgments
Funding: This work was funded by the National Science Foundation grant CBET 2320716 (S.L.)., the National Science Foundation grant CMMI 2338747 (S.L.)., the National Science Foundation grant CBET 2414719 (C.W.)., the National Science Foundation grant CMMI 2301461 (C.W.)., the National Institutes of Health grant R56DE024796 from the National Institute of Dental and Craniofacial Research (H.S.)., and the National Institutes of Health grant 1R01AI186092 from the National Institute of Allergy and Infectious Diseases (J.D.C.). **Author contributions:** Conceptualization: T.H.W., W.L., X.L., H.S., C.W., and S.L. Methodology: T.H.W., R.L., W.L., J.L., Y.C., K.J.K., J.D.C., J.M. Investigation: T.H.W., R.L., W.L., J.L., Y.C., K.J.K., J.D.C., and J.M. Visualization: J.M., T.H.W., W.L., and J.L. Supervision: C.W. and S.L. Writing—original draft: T.H.W., W.L., H.S., C.W., and S.L. Writing—review and editing: T.H.W., W.L., J.L., J.M., X.L., H.S., C.W., and S.L. **Competing interests:** W.C., S.L., T.H.W., and W.L. are inventors on a patent application (pending) submitted by Texas A&M University and Michigan State University, which covers the hydrogel-integrated TNF-α biosensor technology reported in this study. The authors declare that they have no other competing interests. **Data and materials availability:** All data and code needed to evaluate and reproduce the results in the paper are present in the paper and/or the Supplementary Materials. The TAHM biosensor can be provided by S.L. or C.W. upon scientific review and a completed material transfer agreement. Requests for the TAHM biosensor should be submitted to the Michigan State University Innovation Center.

Submitted 11 May 2025
Accepted 19 December 2025
Published 16 January 2026
10.1126/sciadv.ady9180